Detection of Subsurface Defects Using X-Ray Lateral Migration Radiography – A New Backscatter Imaging Technique

Final Report
U.S. Department of Energy
Idaho Operations Office
Grant Number
DE-FG07-00ID13922

By

Edward Dugan
Alan Jacobs

NUCLEAR AND RADIOLOGICAL ENGINEERING DEPARTMENT
UNIVERSITY OF FLORIDA
Gainesville, FL 32611
February, 2003

ACKNOWLEDGMENT:

DISCLAIMER:

Any opinions, findings and conclusions or recommendations expressed in this material are those of the authors and do not necessarily reflect the views of the Department of Energy

DETECTION OF SUBSURFACE DEFECTS USING X-RAY LATERAL MIGRATION RADIOGRAPHY – A NEW BACKSCATTER IMAGING TECHNIQUE

Abstract

A new Compton X-ray backscatter imaging (CBI) technique called lateral migration radiography (LMR), recently developed for the challenging task of detecting all-plastic buried land mines, is applied to detecting a class of sub-surface defects in materials and structures of industrial importance. These include flaws and defects for which there is either no known method or an effective method for detection. Examples are delamination in layered composite structures, defects in deposited coatings on metal surfaces such as in aircraft jet engine components and geometrical structural/composition changes (e.g. due to corrosion) on the inside of shell-like components with only outside surface area access. Measurements and Monte Carlo calculations performed at the University of Florida indicate that LMR should be able to discern defects down to the tens of microns range.

Research efforts include: the construction of simulated flawed test objects on which experimental measurements are performed to establish LMR flaw detection capabilities; performance of Monte Carlo simulations of these measurements to assist in predicting optimum source-detector configurations and to help obtain a detailed understanding of the physics of lateral migration in small voids and how this impacts the resulting LMR image contrasts; the procurement of samples of materials of industrial importance with flaws and defects; the application of LMR to the detection of flaws and defects in these samples; the development of a multi-detector scanning system to provide for faster, more effective flaw detection; and a determination, for the types of samples examined, of the limits and capabilities of flaw detection using LMR.

LMR imaging experiments on the machined samples showed that the optimum contrast in flaw-to-background signal intensity occurred at an X-ray energy of 75 kVp for the aluminum samples and at 35 kVp for the Delrin sample. Monte Carlo simulations and experimental measurements on the aluminum samples showed that LMR is capable of detecting defects down to the tens of microns range. Measurements on the aluminum samples also showed that LMR is capable of detecting relatively small composition variations; a 30 % difference in intensity was observed for aluminum samples that had a few percent difference in iron and copper content.

LMR scans on the aircraft samples showed that LMR is definitely capable of detecting corrosion. Intensity decreases of up to 25 to 30 % were observed in corroded areas relative to intensities in clean areas. Especially significant were scans of samples that were performed with the clean or uncorroded side facing up. The corrosion on the opposite side of these 2 mm thick samples, where there was contact between the frame member and the aircraft skin, was clearly visible. This demonstrates that LMR is capable of picking up composition changes on the inside of shell-like components with only outside surface area access. Scans of other samples showed that LMR is capable of detecting small flaws on the inside of shell-like components with only outside surface area access. Cracks around a fastener hole that were ~ 15 mm in length and no more than 0.25 mm in width were seen through the aircraft skin. Scans of an aluminum honeycomb structure demonstrated that LMR is also capable of picking up internal defects that include crushed core and debonding zones.

Table of Contents

Introduction

A new Compton X-ray backscatter imaging (CBI) technique called lateral migration radiography (LMR), recently developed for the challenging task of detecting all-plastic buried land mines, is applied to detecting a class of sub-surface defects in materials and structures of industrial importance. These include flaws and defects for which there is either no known method or an effective method for detection. Examples are delamination in layered composite structures, defects in deposited coatings on metal surfaces in aircraft jet engine components and geometrical structural/composition changes (e.g. due to corrosion) on the inside of shell-like components with only outside surface area access.

The LMR approach is based on image contrast generated by migration of the X-ray probe radiation in directions transverse to the illumination X-ray beam. Thin, but long, large density variations, such as cracks, and delaminations, generate sufficient signal-to-background ratios to produce images that are not even detectable in the usually interrogated thin dimension. Scaling from the centimeter resolution employed in land mine detection to the sub-millimeter resolution required in many non-destructive examination applications is accomplished by a reduction in the X-ray beam spot size through collimation and a reduction of the X-ray source energy. Typically, for the examined materials, X-ray generator voltages of the order of 50 to 100 kilovolts are required.

Background

LMR was first applied at the University of Florida to the detection of buried land mines. The resulting images were stunning in their definitive detail. The signatures are so unique, that not only can mine detection be accomplished, but also mine identification. The key aspect of the mines that led to these vivid images was the presence of the interior air volumes (due to fuse wells and/or void regions for blast direction). Image intensity signals were in the range of 20 to 300 percent of the background (soil) image. In the land mine search enterprise, such positive detection is rare and justified the construction and field-testing of a small, mobile LMR land mine detection system under U.S Army funding.

It was proposed to exploit the origin of the impressive contrast in LMR land mine images, i.e. voids or air spaces, for the detection, by imaging, of a class of subsurface defects in materials and structures of industrial importance. The LMR approach is based on image contrast generated by migration of the probe X-ray radiation in directions transverse to the illumination radiation beam. Thin, but long, large density variations, such as cracks and delaminations, generate sufficient signal-to-background ratios to produce images of features which are not even detectable in the usually interrogated thin dimension. The detection and imaging of subsurface material defects and geometrical structural changes (e.g. due to corrosion or chemical reaction) on the inside of a shell-like component with only outside surface area access is possible because LMR is sensitive to mass density and atomic number variation in the photon lateral transit paths. Mass

density variation across a crack or delamination is an extreme situation offering significant LMR image contrast.

In the land mine detection situation both detector efficiency and image contrast mechanisms are important. For application to NDE of materials or structures, high detector efficiency and large area detector arrays are not necessarily required, but the physical explanation of contrast dictates the nature of the materials or structure defect that can be (successfully) interrogated. Monte Carlo simulations were performed in support of the experimental measurements in order to obtain a more complete understanding of the transport physics associated with lateral migration in voids. Monte Carlo simulations of the landmine detection problem helped provide an understanding of the physics of lateral migration and the LMR image formation process. However, there are significant differences in the details of lateral migration in the (relatively) large voids in land mines as compared to the small voids typically associated with flaws and defects.

Figure 1 is a simplified schematic illustrating the LMR flaw detection experimental setup. The X-ray source collimator tube is used to define the size or diameter of the probe beam and to a degree, the resolution of the scan. The sample to be examined rests on the sample table of the moving platform assembly. The scan pattern and irradiation time per pixel are computer-controlled. Two types of detectors can be employed. Uncollimated detectors respond primarily to single-scatter photons and provide surface or near-surface information. These signals are easily corrupted by surface clutter or surface inhomogeneities sometimes making it very difficult to detect sub-surface defects. Collimated detectors respond primarily to multiple collision photons. These signals, although much less intense than those reaching the collimated detector, are less easily corrupted by surface clutter and generally provide a much higher signal-to-noise ratio than uncollimated detectors. Figure 1 shows a collimated detector. The length of the lead collimator is sized to just clip out single-scatter photons. Important distances include the source beam-to-detector distance, the height of the detector above the sample, the collimator length and the height of the X-ray source above the sample. Also important are the beam size (diameter), the pixel irradiation time and the X-ray generator voltage and current.

It should be emphasized that it is not necessary to have continuous (delamination) defects nor to use a beam size which yields sufficient resolution to image each defect. An average over several defects will indicate flaw (delamination) presence, and the blurred image will locate the position of a group of defects as well as their cumulative extension. Measurements and Monte Carlo simulations show that LMR is capable of yielding signal contrasts of 5 % for defects of the order of tens of microns.

Experimental Facility

Figures 2 through 5 show different views of the lateral migration radiography experimental facility. Figure 2 is an overall view of the facility. Located in the top, middle region of the green Unistrut support frame is the cylindrical, horizontally-mounted Lorad X-ray generator. The generator is wrapped in lead. The silver, perpendicular x and y

tracks fastened to the plywood platform on the floor are part of the Motionex table which controls the x, y and z positioning of the scanned sample. The three identical, vertical boxes in the foreground on the plywood platform are the controllers for the three stepper motors that provide the Motionex table movement in the x, y and z directions. The Motionex table has sub-millimeter positioning accuracy and is used to move the sample during the LMR scanning according to a user-specified pattern. The Lorad LPX 200 is a compact, state-of-the-art, constant potential, liquid-cooled X-ray generator. The X-ray output range is 10 kVp to 200 kVp at 0.1 mA to 10.0 mA with a 900 watt maximum power level. The green box in the back corner of the room is the heat exchanger unit for the X-ray generator.

Figure 3 shows the X-ray generator source beam vertical, brass collimator tube extending down from the bottom of the X-ray generator and through the plywood detector mounting board. The sample table, below the bottom of the brass collimator tube, is connected to the Motionex table below (see Figure 2) to form the moving platform assembly. To the left and right of the bottom of the brass collimator tube are two cylindrical, horizontally-mounted sodium iodide scintillator detectors. A third sodium iodide detector is located behind the brass collimator tube and is oriented perpendicularly to the other two detectors. The detectors are wrapped in lead and up to four sodium iodide scintillator detectors can be used during the scanning process. Figure 4 shows one of the sodium iodide detectors without the lead wrapping. A LabVIEW program was written to control the Motionex table scanning movement and the detector data acquisition process.

Figure 5 is a close-up of the bottom of the brass collimator tube and the three sur-rounding sodium iodide detectors. In some of the image scans presented later, reference is made to different detector numbers. In this photograph, detector 3 is on the left, detector 2 is on the right and detector 1 is oriented perpendicular to these two detectors and located behind the brass collimator tube. One of the aluminum sample plates appears below the detectors on the sample table. The lead detector collimators can be seen on the inner ends of the two detectors located to the left and right of the brass tube. The detectors are surrounded on all sides by lead except for a small opening on the bottom of the detector.

Description of the Image Acquisition System

The Flaw Detection Image Acquisition System consists of four principal units:
- An industrial X-ray generator
- A moving platform assembly
- Radiation detectors and associated counting devices
- A PC that controls the image acquisition process

The following is a description each of the latter three elements.

6

<u>Moving platform with motion controller</u>

The flaw detection image acquisition process requires the target to be moving under an X-ray beam (the X-ray generator is static). The moving platform allows a scanning, 2D (x-y) motion in the plane perpendicular to the X-ray beam as well as the possibility of adjusting the vertical distance between the X-ray generator and the target (sample). In other words, the moving platform assembly can position or move a target in any of the three directions of its three perpendicular axes. Three stepper motors achieve the motion/position along each axis. These motors are fully controllable with a motion controller that constantly reads the position of the motors with on-board encoders. This motion controller can be programmed or controlled "on-the-fly" by a computer through a RS232 connection and ASCII messages. More specifically, LabVIEW builds the strings and communicates with the controller. The controller allows a large number of operating modes and settings and the accuracy of the position/motion of this platform well exceeds the requirements of these experiments. The platform is equipped with safety magnets that alert the controller when motion along an axis is reaching the end of its range. An over-current protection automatically shuts down the controller when one of the axes gets stuck. The risk of damaging the equipment is therefore greatly reduced during operation.

<u>Detectors and counting devices: Ranger</u>

The setup is equipped with up to four Na-I detectors that emit light when penetrated by a photon backscattered by the target. A photo-multiplier on each of the detectors then intensifies this light. High voltage units power the photo-multipliers and allow the signal to be transformed into voltage. This signal then enters a pulse-processing unit that fits the signal before the counting process. The counter is the measurement device of this setup: it counts the number of photon backscattered into the detectors in a given amount of time. This counter or "Ranger" card is actually a PC card located within the computer and connected to the output of the pulse processing unit. The counter is fully programmable, has its own independent timer and can store a significant amount of data. LabVIEW communicates with it by sending and receiving bytes directly on the PC internal data bus.

<u>Computer platform: LabVIEW</u>

A standard PC equipped with LabVIEW is the user interface of the image acquisition set-up. The computer communicates with the motion controller and the Ranger, inputs the user data and displays the results. LabVIEW was the software of choice to integrate these operations.

Image acquisition process

The concept of image building is simple. The target object is moved to a specific location underneath the X-ray beam. The number of photons backscattered into the detector is then counted during a fixed amount of time. The photon count is converted into a color that is applied to the pixel corresponding to the target location. The platform is then

moved to its next location and the process continues. This method was the one applied initially with the single detector system and gave very good results though it wasted a considerable amount of time by waiting during the platform movement between two pixel locations. The new acquisition method, described below under *Data Acquisition*, is faster and delivers an image of greater quality.

Input

The first required operation is to move the center of the target object right underneath the X-ray beam. This center will also be the center of the image.

The user can then enter the dimensions of the image that define the area to be scanned. The user also sets the pixel dimensions that affect the quality of the image and the number of scan sweeps. The X-ray beam diameter is saved for future reference but does not affect the image acquisition process.

Next the user sets the amplitude filter of the counter. Two modes are available: Integral mode which filters any pulse smaller than a threshold value and an SCA mode which only counts pulses whose amplitudes are located within a window above a threshold value.

Finally the exposure time needs to be set. This exposure time is the counting period corresponding to one pixel.

The setup is then ready and the scanning can start as soon as the X-ray machine is enabled.

Data acquisition

The Ranger has an embedded memory that can store a large amount of data. In a continuous acquisition mode, the counter counts pulses during a given amount of time, stops, stores the data in memory, and waits another period of time before automatically starting again. The counting data automatically fills up the memory in this manner while the computer reads and empties the buffer. If the target moves continuously during the data acquisition, a new line can be added to the image without stopping the stepper motors or the counters. This results in a faster scanning and allows a greater number of pixels at no additional "cost".

When data acquisition is started, both the motion controller and the Ranger card are re-initialized and the appropriate settings configured. The scan sweeps occur "horizontally" or "vertically" (with reference to the image) depending on the dimensions input by the user. The moving platform then automatically moves to its starting position and starts scanning immediately. Each new image line is acquired in the fashion described above: many counts are stored in the Ranger memory while the target moves underneath the X-ray beam. The computer continuously reads and empties the data buffer. This operation allows the acquisition of more data points than the Ranger can store. This data is immedi-

ately converted and the image updated. The moving platform then moves to the starting position for the next scan sweep. Since the Ranger and the motion controller are two independent platforms, the only synchronization event is generated by the computer and occurs at the beginning of each scan sweep. Once the given number of sweeps is reached, the moving platform goes back to its initial location and the computer saves the images.

Output

The images are continuously displayed and updated in a LabVIEW window. The user is informed of the duration of the scan and provided with an estimate of the remaining time. The output of the image acquisition process is a set of JPEG images and text files that contains the counts in a matrix format. Another text file contains the system settings input by the user.

Image processing and filtering

Even though the program described above outputs JPEGs images, additional image processing may be required like zooming, filtering, interpolation or simply increasing the size of the output image.

A LabVIEW based program allows all these operations by asking the user for the text files that contains the data in ASCII format. Additional information like the pixel dimensions is automatically extracted from a support file or can be input manually. The number of columns and lines stored in the input file give the number of columns and lines of the image. This information is then extracted and the initial image is built. At this point the operator can select the portion of the image he wants to keep for additional processing. This is the typical way of zooming in on an image's features.

One image may look "raw" if the number of photons captured in one pixel is small. Since the error associated with a count N is $\sqrt{N}$, the error can be rather large for small values of N. The filtering concept is simple: if a pixel value is averaged with the value of its neighbors, its associated error is reduced. The filtering program was developed using C++ and interfaced with LabVIEW. This program includes three filters. Two inputs for these three filters are identical: the input image, in the form of an array of numbers, and the dimensions of an averaging window. For a given pixel, the filter computes the average of all the pixel values contained within the window that is centered on the pixel. The filters differ in the weight distribution given to the neighbors in the averaging process.

- The most basic filter is called a "rectangular window". It gives the same weight to all pixels in the averaging process.

- The second filter is an adaptive filter. This means that if the error associated with a given pixel is below a user-defined threshold, the filter will not do anything. Otherwise, an averaging process will occur. The goal here is to avoid unnecessary

filtering. It is well known that averaging reduces the error but it also removes small features or smooths-out an image. Since the error for each pixel is known, this error can be compared to a threshold value. If the error is larger than the threshold, the pixel is averaged with an increasing number of neighbors thereby reducing the error. If the error is smaller than the threshold, there is no averaging and small features do not vanish from this section of the image. The process is simple. The first comparison is between the threshold value and $\sqrt{N}$. If $\sqrt{N}$ is too big, the value of the pixel, as well as its error, are recalculated after an averaging that uses the first neighbors around the pixel. A new comparison occurs and the averaging process stops or continues to the second, third, fourth… neighbors. The number of neighbors defines the order of averaging: an averaging that uses up to four neighbors has an order of four. The process stops when the error is smaller than the threshold or when the size of the averaging window is reached. If a very small threshold is chosen this filter and the one described previously are really identical: the averaging occurs until the maximum size of the averaging window is reached.

- The third filter is also an adaptive filter and is identical in principle to the one described above. However, it uses a weight that has a Gaussian-like shape: the weight of a neighbor in the averaging process depends on its distance from the center pixel and follows a Gaussian curve. This way, more importance is given to the pixels closer to the center pixel and less importance to the ones away from it.

The adaptive filter is very beneficial in the case of filtering an image with a small feature in a mountain (large N) with lots of noise in the valleys (small N). A regular averaging would smooth out equally every pixel of the image, hiding the small features. In contrast, the adaptive filter will not filter out the mountain because the error there is much smaller than the error in the valley where most of the filtering would occur.

Once the appropriate filtering is achieved the user has the option of choosing the size of the final JPEG image, its orientation, the presence of scales or even additional interpolation. The output image as well as the input image, error image and order images can also be saved.

Flaw Samples

A number of industrial samples were obtained containing various flaws and defects. Four other samples were machined with selected size flaws; three of the samples were made of aluminum and one of Delrin plastic.

Figure 6 shows an aircraft composite pressure bulkhead piece that has delaminations. The dimensions in the figure are in millimeters and this item is labeled Sample #1.

Figure 7 shows an aircraft wing trailing edge piece with corrosion in the marked area. Dimensions are again in millimeters and this piece is designated Sample #2. Figure 8 shows an aircraft fastener piece with a crack at the marked hole. This is labeled Sample #3. Figure 9 is a picture of an aircraft skin sample that has no flaws; it is marked as Sample #4.

Figures 10 and 11 show two aircraft frame members in which there was corrosion between the aircraft skin and frame member. These are designated Sample #5 and Sample #6, respectively.

Figure 12 shows Sample #7, a Boeing composite piece, with flaw and defect status unknown. Figure 13 shows an aluminum honeycomb panel with a series of defects that are marked in Figure 13a. This is designated Sample #8.

Figure 14 shows samples from a Pratt and Whitney turbine blade casing with a number of flaws and defects in the deposited coatings on the metal surface, as marked. This is Sample #9. Figure 15 shows a General Motors cast aluminum piece that has been formed with a technique that is being looked at to manufacture engine blocks. There have been problems with defects of unknown origin in these pieces. This is designated Sample #10; there were a dozen of these cast aluminum pieces.

Figures 16 through 19 show schematics of the three aluminum flaw plates that were machined. There was also a flaw plate machined from plastic (Delrin) that has dimensions which are essentially those of aluminum flaw plate #1 shown in Figure 16.

Discussion of Results

An very large number of images of the various samples identified above were obtained during this research effort. Many of these scans were acquired during measurements performed to obtain optimum configurations, including optimum X-ray generator settings, optimum source-to-sample distance or detector collimator length and optimum detector position. The image results presented and discussed below are but a small fraction of the total collection of acquired images. The results presented were selected to provide a representative illustration of the capabilities of LMR, as determined in this research, to detect subsurface flaws and defects in materials. In some instances, no results of interest were obtained. For example, six of the General Motors cast aluminum pieces were scanned multiple times and no flaws or defects could be found. It was unknown whether any of these particular samples contained any defects. Because these were not our samples to keep, destructive examination to verify the LMR scan results was not an option.

Sample #1

Sample #1 is the composite pressure bulkhead piece that is shown in Figure 6 with the "labeled side" of the sample facing up. Two scans of Sample #1 are presented and the

locations of these two scans are indicated in Figure 6. These two images were taken with the three-detector system using the "new" image acquisition process. The pixel size for both images was 1 mm x 1mm.

Figure 20 shows a 90 mm by 60 mm scan of Sample #1 centered about Location 3. The scan was done with the labeled side of the sample facing down. The high intensity region in the lower left corner of the Figure 20 image corresponds to the sloped region in the left rear corner of the Location 3 area in Figure 6 where the thickness of the sample decreases. Within the thicker central composite region, where the intensity generally shows as purple, the higher intensity, blue region (along $y = 30$, from about $x = 20$ to $x = 90$ and along $x = 30$, from $y = 30$ to $y = 60$) is a flawed region in the composite. This scan was done with a 2 mm X-ray beam spot size and with the X-ray generator operating at 60 kVp and 5.7 mA.

Figure 21 is a 98 mm by 24 mm scan centered about Location 6 along the thinned region where the top and bottom layers encasing the composite are joined together and the image shows the details of this seam. The image was acquired with the labeled side of the sample facing up. The X-ray beam spot size was again 2 mm and the X-ray generator was operated at a reduced voltage of 50 kVp and at a reduced current of 5.5 mA in this thin region.

Sample #2

Three areas of Sample #2, the trailing edge of a wing, were scanned. Figure 22 identifies the three areas. Figure 23 presents the images from the first two scans. These scans were done using the single-detector system and the old image acquisition process. Scan 1 is of a clean area. The honeycomb-like internal structure can be clearly seen and the background intensity around the circular, low intensity blue areas falls off from left to right as shown with the red to green color change. The intensity decrease is due to the decreasing thickness of the sample as the scan goes from left to right. The circular void areas in the honeycomb structure show up as low (blue) intensity because an absorbing lead sheet was placed below the sample on the sample table. Scan 2 is also of a good area, but note that the background intensity is now all red due to the greater thickness of the sample here as compared to the Scan 1 area.

The pixel size for Scans 1 and 2 is 1 mm x 1mm and the scans include 400, or 20 x 20 pixels. The scan time for each pixel was 0.5 seconds. The x-ray generator voltage was 75 kilovolts with a current of 9 milliamps and the detector was operated at 800 volts. The lower level of the discriminator setting (lld) for the counting system is 0.4 and the counting system window is 9.6. The lower level window setting prevents the signal from being contaminated with low energy background (noise) photons and the upper level setting, determined by the window size, eliminates contributions from spurious high energy (e.g. cosmic) radiation. The hole size at the end of the brass, source beam collimator tube was 2 mm in diameter and the length of the brass source beam collimator

tube was 25 cm. The vertical distance from the x-ray source to the sample for Scan 1 was 75 mm. For Scan 2 the vertical distance from source to sample was 80 mm.

Sample #2 was also scanned using the three-detector system and the new image acquisition process. The area scanned is identified as scan region 3 in Figure 22. Figure 24 shows the scan of this region with the labeled side of the sample facing up. The red vertical strip at about x = 6 to x = 7 is a region of internal corrosion. The red spot centered at x = 27 and y = 12 is a cell with water and the green area is a region of crushed core. Figure 25 is a scan of approximately the same area, but taken with the labeled side of the sample facing down. The red vertical strip marking the internal corrosion region is now at x = 0, the red spot marking the cell with water is now at x = 22 and y = 36. The green area marking the crushed core region is still clearly visible. The pixel size for both of these images was 1 mm x 1 mm. The X-ray source beam spot size was 2 mm and the X-ray generator was operated at 55 kVp and 5 mA.

Sample #3

Figures 26 through 28 show images of Sample #3 obtained with the three-detector system and the new image acquisition process. The area scanned is the region marked with the blue lines in both Figure 8 and in Figure 26b. The side of Sample #3 facing up during the scan results presented here is the side shown in Figure 26b; the side with the blue lines shown in Figure 8 was facing down. The photograph of Sample #3 in Figure 26b has a magnification of about 2x actual size. The actual center-to-center distance between the two fastener holes is 28 mm and the diameter of the holes is 6 mm.

The unprocessed image in Figure 26a clearly shows the cracks located to the right of the left fastener hole. The maximum width of the largest of these three cracks is 0.25 mm. The fastener holes in these images show an increased intensity because the fastener was mounted on a wood block. A lead sheet was placed underneath the wood block Figure 27 shows a processed image, but taken at different system settings. Relative to the image in Figure 26, the crack detail is not as sharp. This is because the detector collimator length and X-ray generator voltage settings used here are the same as those used to image Sample #3 when it was covered by an aluminum skin. Sample #4 (see Figure 9) provided the aluminum skin used to cover Sample #3 and Figure 28 shows the image obtained with the aluminum skin covering this frame piece. Although the crack detail is now somewhat blurred, the crack presence is still very obvious. This result demonstrates that LMR is capable of picking up small flaws on the inside of shell-like components with only outside surface area access. Note that for the set of images of Sample #3 the X-ray beam spot size was reduced from the previously used 2 mm to 1 mm and the pixel size was reduced from 1 mm x 1 mm to 0.5 mm x 0.5 mm.

Three scans were done of Sample #5, which had corrosion between the skin and frame member, using the single detector system and the old image acquisition process. Figure 29 shows these scanned areas for Sample #5. Scan 1 in Figure 29 includes a large area of corrosion in the right portion of this 50 x 50 pixel scan. There is a significant decrease in intensity (green) in the corroded area compared to the red background intensity. The fastener holes show up blue (low intensity) because of the lead sheet that has been placed underneath the sample.

Figure 30 presents Scan 2 and Scan 3 of Sample #5. These are 20 x 20 pixel scans and the vertical distance from source to sample is 72 mm, the same as for Scan 1. Scan 3 is of a clean area, with the fastener hole clearly visible. Scan 2 is of a corroded area, and at first glance this looks like the high intensity (red) areas in Scan 3 and in the left side of Scan 1. However, the high intensity areas in Scan 1 and Scan 3 have around 3000 counts and higher. The red area in Scan 2 has only about 1800 to 2000 counts which is the same as for the lower intensity (corroded) green area in Scan 1.

Sample #5 was also scanned using the three-detector system and the new image acquisition process. The scanned area is approximately the region marked with the blue lines in Figure 10. Figure 31 presents this image. The top horizontal blue line in Figure 10 corresponds to the bottom of the image in Figure 31 and the bottom horizontal blue line in Figure 10 corresponds to the top of the image in Figure 31. Thus, the corroded region, which is on the right of the scanned area identified in Figure 10, is on the left in the image in Figure 31. There is more detail in the image obtained with this new system as compared to the images obtained with the old system (Figures 29 and 30). However, as before, the corroded area shows up with a lower (green and blue) intensity than the uncorroded areas (yellow and red). For this image, the X-ray beam spot size was back at 2 mm and the pixel size was back at 1 mm x 1 mm. The X-ray generator voltage for all four of the Sample #5 images was 75 kVp; the current setting was 9 mA for the first three images and 8.5 mA for the fourth image.

Sample #6

Two scans were done of Sample #6, which also had corrosion between the skin and frame member, using the single detector system and the old image acquisition process. These scanned areas are shown in Figure 32. Figure 33 shows Scan 1 and Scan 2. Scan 2 is of a clean area with two fastener holes. This is a 30 x 30 pixel scan. Scan 1 includes a significant region of corrosion. In Figure 32, the corroded area is to the right and the clean area to the left. The Scan 1 image in Figure 33 has 50 x 50 pixels and is rotated 90 ° clockwise relative to the orientation of the scan region marked in Figure 32 as can be seen from the position of the fastener holes. The right, corroded area in Figure 32 is the green, low intensity area at the bottom in Figure 33. The left, clean area in Figure 32 is the red, higher intensity area at the top in Figure 33. The blue, low intensity area at the very top of Scan 1 in Figure 33 is due to some of the scan area extending

beyond the sample (to the left of the sample in Figure 32). The vertical distance from source to sample for both these scans was 65 mm.

The Scan 1 results for Sample #6 clearly demonstrate that LMR is able to detect areas of corrosion when the side containing the corrosion is face up. A more difficult, and more significant, test is to be able to detect the corrosion when the corroded side is face down and the opposite or reverse side (which is clean and un-corroded) is face-up. Figure 34 presents results for this case. The higher intensity, red and red-orange regions that include the right, top and bottom portion of the image is the good or un-corroded area of the frame member scan. Because the scanning was from the reverse side, the right side of the image corresponds to the left side of the delineated scan zone in the frame member photograph. The lower intensity, yellow region in the center left side of the image is the corroded area. The intensity difference between the corroded and uncorroded regions is 15 to 20 %. The corroded area is seen clearly even when this 2 mm thick frame member is scanned with the opposite (or good) side facing up. This result demonstrates that LMR is capable of picking up composition changes on the inside of shell-like components with only outside surface area access. This capability is also seen in the scan results for Sample #2 (Figures 24 and 25).

Sample #6 was also scanned using the three-detector system and the new image acquisition process. The scanned area is approximately the region marked with the yellow lines in Figure 32. Figures 35 and 36 present the scan images. Figure 35 shows the image obtained when the scan was done with the labeled (corroded) side facing up. The image is rotated clockwise 90º relative to the orientation shown by the marked region in Figure 32. The corroded area has a lower intensity (dark blue) than the uncorroded areas. Although the corroded area shows clearly, the contrast would be sharper if the X-ray gen-erator voltage were reduced slightly and/or if the detector collimator length was slightly reduced. Settings used for this scan were those that also allowed corrosion to show well when the sample was scanned with the unlabeled or the good side facing up. Figure 36 shows the image obtained with the labeled or corroded side facing down. Once again, the corroded area with the lower (blue) intensity is clearly seen even when this 2 mm thick frame member is scanned with the clean side facing up. These two images were obtained with an X-ray beam spot size of 2 mm and the X-ray generator operating at 75 kVp and 8.5 mA.

Sample #8

Three scans were done of Sample #8, which is an aluminum honeycomb panel that contains a number of internal defects, using the single detector system and the old image acquisition process. Figure 37 shows Sample # 8 and the scanned areas. (Figure 13 also shows two views of this aluminum honeycomb panel.) A scan of the 1 inch (~25 mm) diameter debonding region is given in Figure 37. This is a 40 x 30 pixel pixel image and the honeycomb structure is clearly visible. The debonding region shows a significant decrease in image intensity. Figure 38 includes a 30 x 30 scan of the 0.5 inch (~13 mm)

diameter debonding region and a 20 x 20 pixel scan of a region that has no defects. For all three of these scans, the source-to-sample height was 85 mm.

Sample #8 was also scanned using the three-detector system and the new image acquisition process. Figure 39 shows an image of the 1 inch (~25 mm) diameter debonding region. The debonding region again shows a significant decrease in intensity and the honeycomb structure is visible in the background. The sharpness and detail of this image obtained with the new system is to be compared with the image of this region obtained with the old system in Figure 37. This image was obtained with an X-ray beam spot size of 2 mm and the X-ray generator operating at 70 kVp and 7.5 mA.

Figures 40 and 41 present images obtained with the new system of the 0.5 inch (~13 mm) diameter debonding region. The image in Figure 40 was taken with the labeled side of the of the sample facing up and the image in Figure 41 was taken with the labeled side facing down. Both images were obtained using a 2 mm X-ray beam spot with the X-ray generator operating at 75 kVp and 9 mA. The honeycomb structure is again apparent and the low intensity (green) area is the debonding region. Figure 42 shows a scan of the crushed core region of Sample #8. For this image, the X-ray generator current was reduced to 8 mA. The high intensity region on the right side of the image is the crushed core region; details of some of the honeycomb structure can be seen in the left side of the image.

Figures 43 and 44 give images of the 0.25 inch (~ 6 mm) diameter debonding region. Figure 43 shows the unprocessed image and Figure 44 presents the processed image. The debonding area is clearly visible in both images. In Figure 44 it shows as the low intensity region centered at x =10 and y = 13. The low intensity vertical line at about y = 18 clearly indicates the presence of some additional, but unknown, internal defect in this aluminum honeycomb panel. Finally, Figure 45 gives a scan of the "film region" of Sample #8. A small piece of film was located inside the honeycomb panel and the LMR scan clearly shows the location of this piece of film. For the images in Figures 43, 44 and 45 the X-ray generator beam spot was 2 mm and the X-ray generator was operated at 75 kVp and 9 mA. All of the scans of Sample #8 with the three detector system and the new image acquisition process used 1 mm x 1 mm pixels.

Figure 46 shows a scan of the central region of the machined aluminum sample plate #2 (see Figure 17). The high intensity region in the image center is the simulated flaw that is 10 mm wide, 0.95 mm in height and located about 3 mm beneath the surface. The image shows about a 20 % increase in intensity at the location of this flaw. Figure 47 shows a scan of the central region of machined aluminum sample plate #3 (see Figures 18 and 19). The region scanned includes the central four of the six simulated flaws and clearly shows the location of all four flaws. These flaws range in size from 1 mm to 5 mm wide, in height from 0.3 mm to 0.5 mm and are located from 2.5 to 2.7 mm beneath the surface.

Concluding Remarks

An experimental facility for LMR flaw and defect detection has been construc-
ted. The facility includes a Motionex movable table with sub-millimeter accuracy in
positioning, a state-of-the art Lorad 200 keV X-ray generator and four Bicron, sodium
iodide, scintillator detectors. The cost of this equipment was about $ 50 K. A LabVIEW
program was written to control the system scanning motion and the detector data
acquisition process. Matlab is used to do data processing and image plotting.

The initial LMR system used for flaw detection had only a single collimated detector and
employed a simple data/image acquisition method. For this process, the sample was
moved to a specific location, the moving platform assembly was stopped and backscatter
photons were counted for a given period of time. This procedure was then repeated,
point-by-point, until the desired image was obtained. A multi-detector system was
developed during the second year of this research along with an advanced data/image
acquisition method in which the sample moves continuously. The new arrangement
resulted in a faster system with higher quality images and more effective flaw detection.

Industrial samples were obtained containing various flaws and defects. These included
aircraft structural and skin pieces, a Boeing composite piece, a Pratt and Whitney turbine
blade casing sample and General Motors cast aluminum pieces. Four other samples were
machined with selected flaw sizes; three of the samples were made of aluminum and one
sample of Delrin plastic.

LMR imaging experiments on the machined samples showed that the optimum contrast
in flaw-to-background signal intensity occurred at an X-ray energy of 75 kVp for the
aluminum samples and at 35 kVp for the Delrin sample. Monte Carlo simulations and
experimental measurements on the aluminum samples showed that LMR is capable of
detecting defects down to the tens of microns range. Measurements on the aluminum
samples also showed that LMR is capable of detecting relatively small composition
variations; a 30 % difference in intensity was observed for aluminum samples that had a
few percent difference in iron and copper content.

LMR measurements on the aircraft samples showed that LMR is definitely capable of de-
tecting corrosion. Scans of industrial samples #2, #5 and #6 clearly showed the areas of
corrosion. Intensity decreases of up to 25 to 30 % were observed in corroded areas
relative to intensities in clean areas. Especially significant was a scan of Sample #6 that
was performed with the   clean or uncorroded side facing up. The corrosion on the
opposite side of this 2 mm thick sample, where there was contact between this frame
member and the aircraft skin, was clearly visible. This demonstrates that LMR is capable
of picking up composition changes on the inside of shell-like components with only
outside surface area access. Scans of Sample #3 demonstrate that LMR is capable of
detecting small flaws on the inside of shell-like components with only outside surface
area access. Scans of Sample #8, an aluminum honeycomb structure, demonstrated that

LMR is also capable of picking up internal defects that include crushed core and debonding zones.

In conclusion, this research has successfully demonstrated that LMR is capable of detecting sub-surface and internal flaws and defects, relatively small composition changes and corrosion in materials and structures of industrial importance. The materials of the examined samples included aluminum, composites and plastic. This research has also demonstrated that LMR can detect corrosion and defects on the inside of shell-like components with only outside surface area access. For the examined samples, optimum X-ray generator voltage was in the range of 50 to 75 kVp.

List of Publications:

E. Dugan and A. Jacobs, Detection of Subsurface Defects Using Lateral Migration Radiography – A New Backscatter Imaging Technique," U.S. DOE NEER grant DE-FG07-00ID13922, Annual Scientific and Technical Report, University of Florida, August, 2001.

S. Brygoo. "X-Ray Lateral Migration Radiography Non-Destructive Flaw Detection Measurements and Simulations." Master's Research Project, University of Florida, May, 2002.

A. Jacobs, E. Dugan, S. Brygoo, D. Ekdahl, L. Houssay and Z. Su, "Lateral Migration Radiography: A New X-ray Backscatter Imaging Technique," Proceedings of SPIE 47th Annual Meeting, Symposium on Optical Science and Technology, Penetrating Radiation Systems and Applications IV, Vol. 4786, pp. 1-16, Seattle, July, 2002.

E. Dugan, A. Jacobs, L. Houssay and D. Ekdahl, "Flaw Detection Using Lateral Migration X-ray Radiography," ASNT 12th Annual Research Symposium, Orlando, March 10-14, 2003.

E. Dugan, A. Jacobs, L. Houssay and D. Ekdahl, "Detection of Flaws and Defects Using Lateral Migration X-ray Radiography," SPIE 48th Annual Meeting, International Symposium On Optical Science and Technology, Penetrating Radiation Systems and Applications V, San Diego, August 3-8, 2003.

Scientific Personnel:

Edward T. Dugan, Ph.D., PI
Alan M. Jacobs, Ph.D., co-PI
Dan Ekdahl, Electronics Technician
Stephanie Brygoo, Graduate Student
Laurent Houssay, Graduate student
Robert Smith, Graduate student
Clay Long, student

Degrees Received:

Stephanie Brygoo, Masters in Nuclear Engineering, May, 2002
Laurent Houssay, Ph.D. in Nuclear Engineering, in progress.

Special Acknowledgment:

David Kessler, QA Technologies, Inc. for providing most of the industrial samples.

Report of Inventions: A patent has been applied for on a related application.

Technology Transfer:

None yet. But because of the successful results obtained in the work performed under this NEER Grant, funding has been obtained to perform work for the National Security Agency through the Office of Naval Research. This work for NSA through ONR will make use of the scientific principles of lateral migration radiography developed for flaw and defect detection under this NEER Grant. In addition, the U.S. Air Force has shown interest in the use of LMR for flaw and defect detection on aircraft components. Results from the work performed under this NEER Grant and are being reviewed by Air Force NDI experts and management at Moody AFB.

Figures
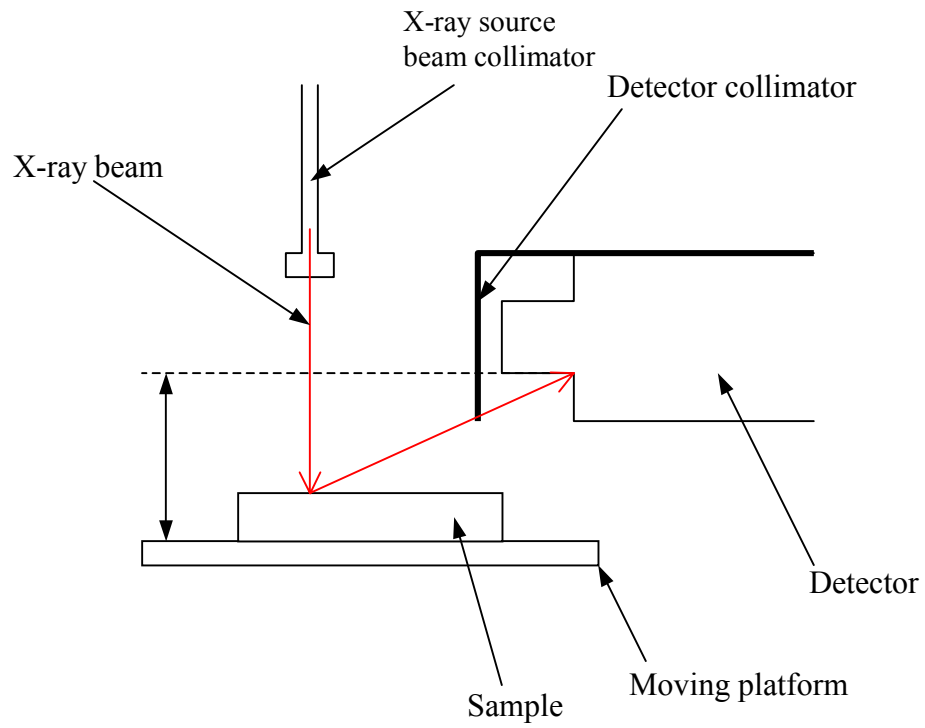
Figure 1.   Simplified schematic of LMR flaw detection experimental setup.

Figure 2. Overall view of the experimental facility.
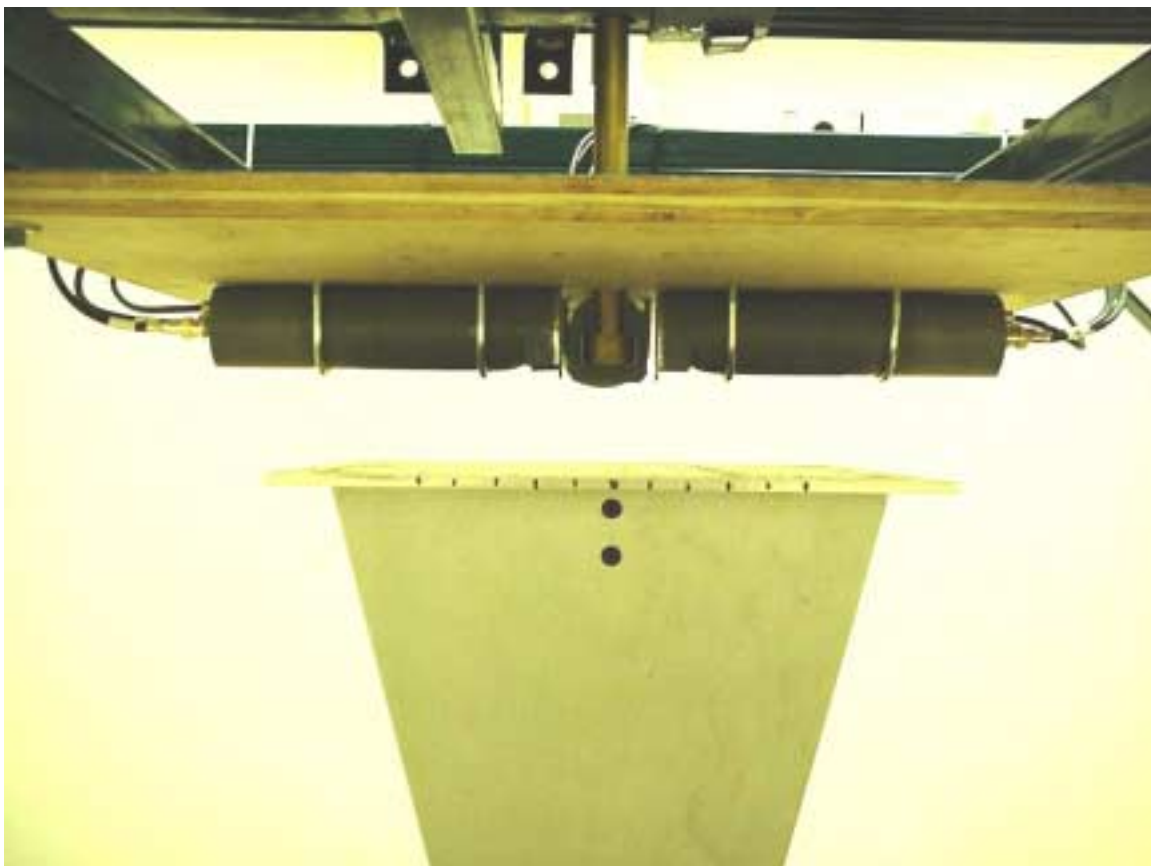
Figure 3. View of sample table, detectors and X-ray source beam brass collimator tube.

Figure 4. Bicron NaI scintillator detector.
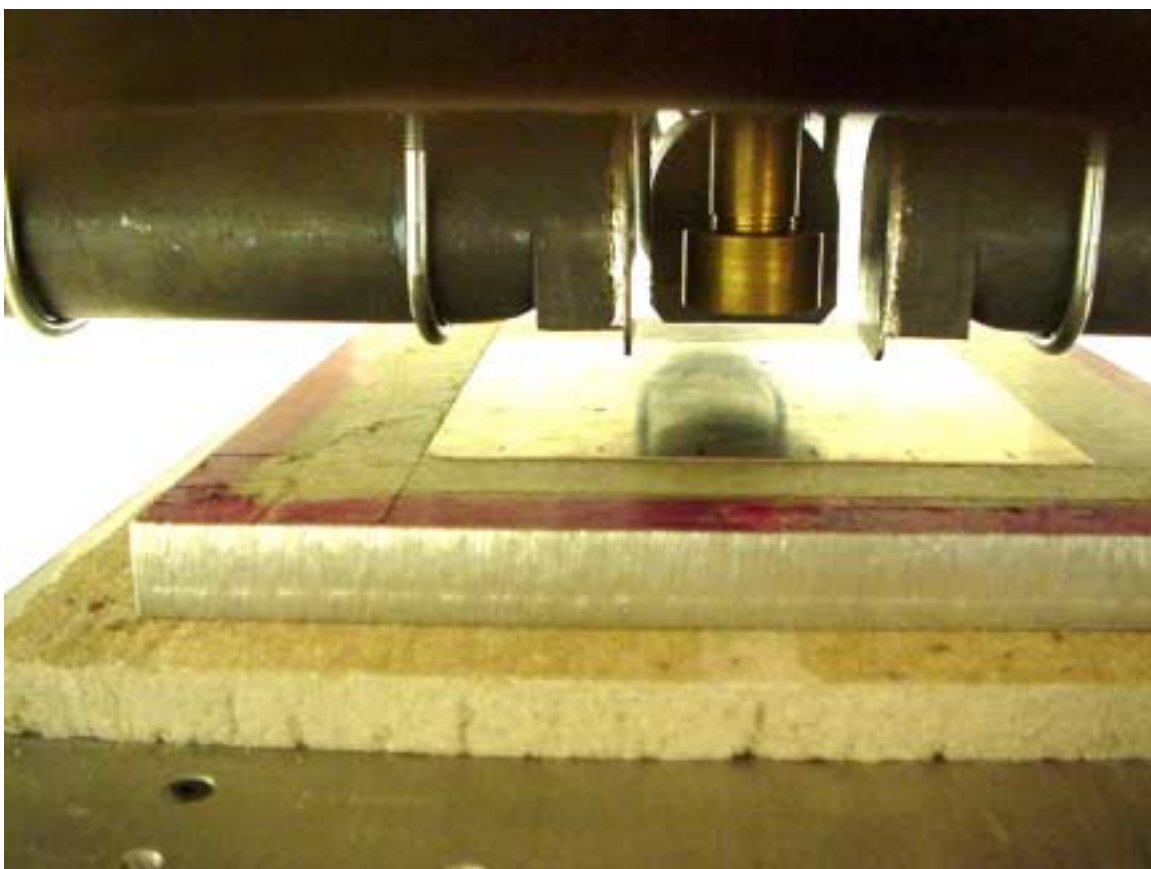
Figure 5. Close-up of the detectors and bottom of the source beam brass collimator tube.
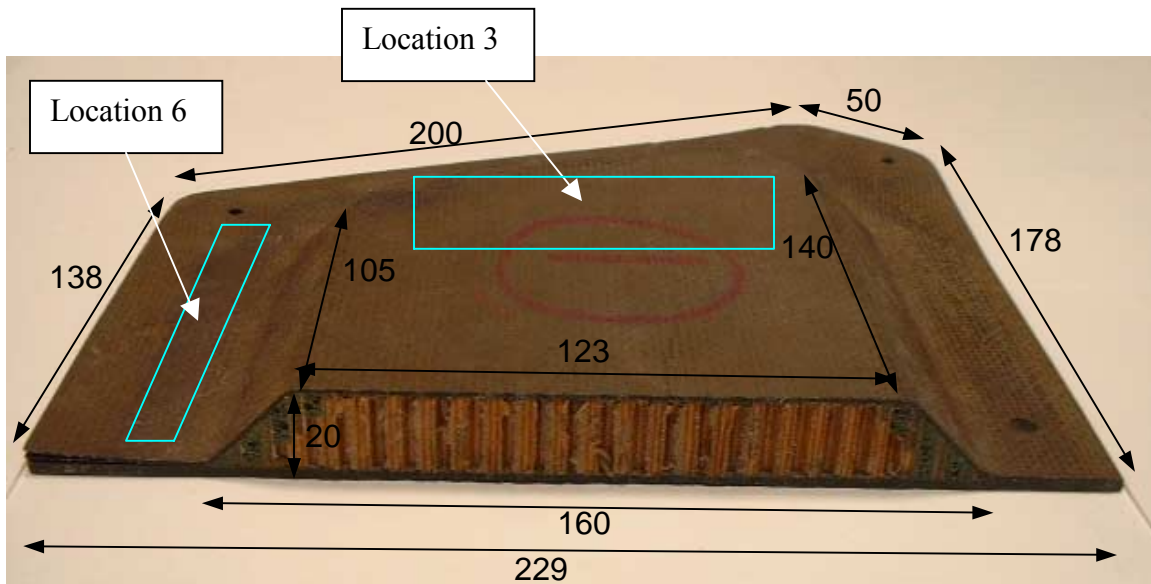
Figure 6. Sample # 1. Composite pressure bulkhead piece.
(numbers give dimensions in mm)
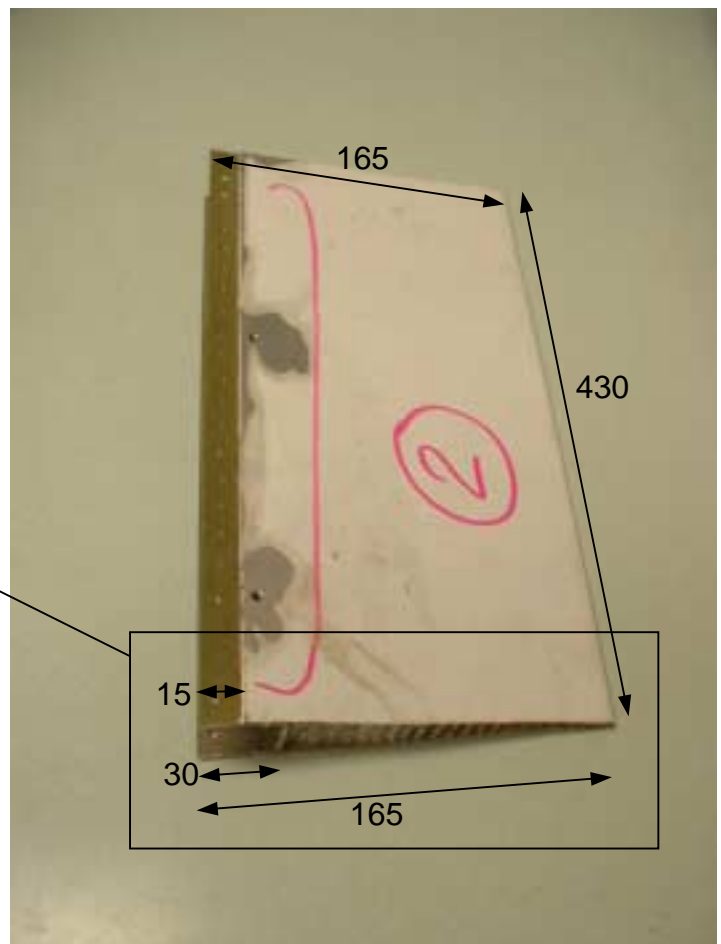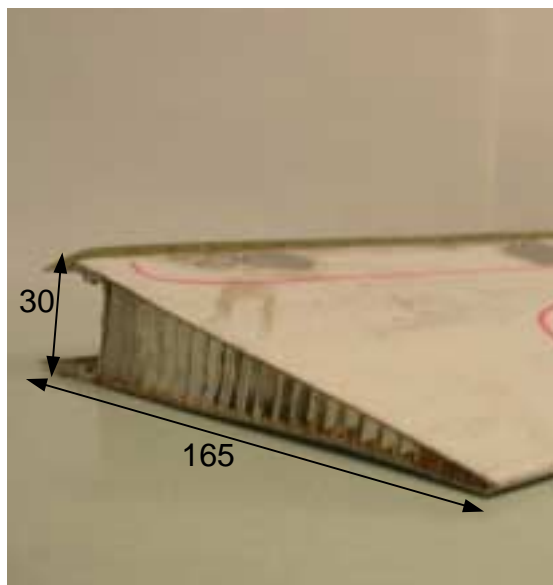
Figure 7. Sample # 2. Trailing edge of wing with corrosion in marked area.

(numbers give dimensions in mm)

26
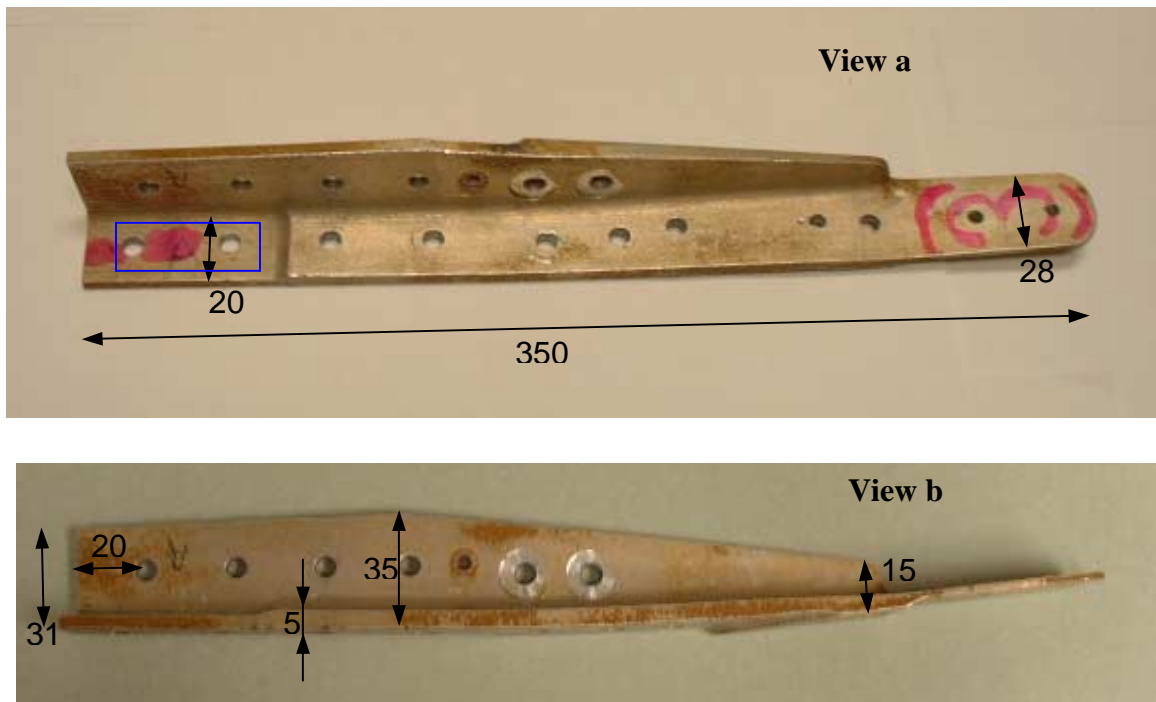
Figure 8. Sample # 3. Crack at fastener hole:
Two different views: a and b.
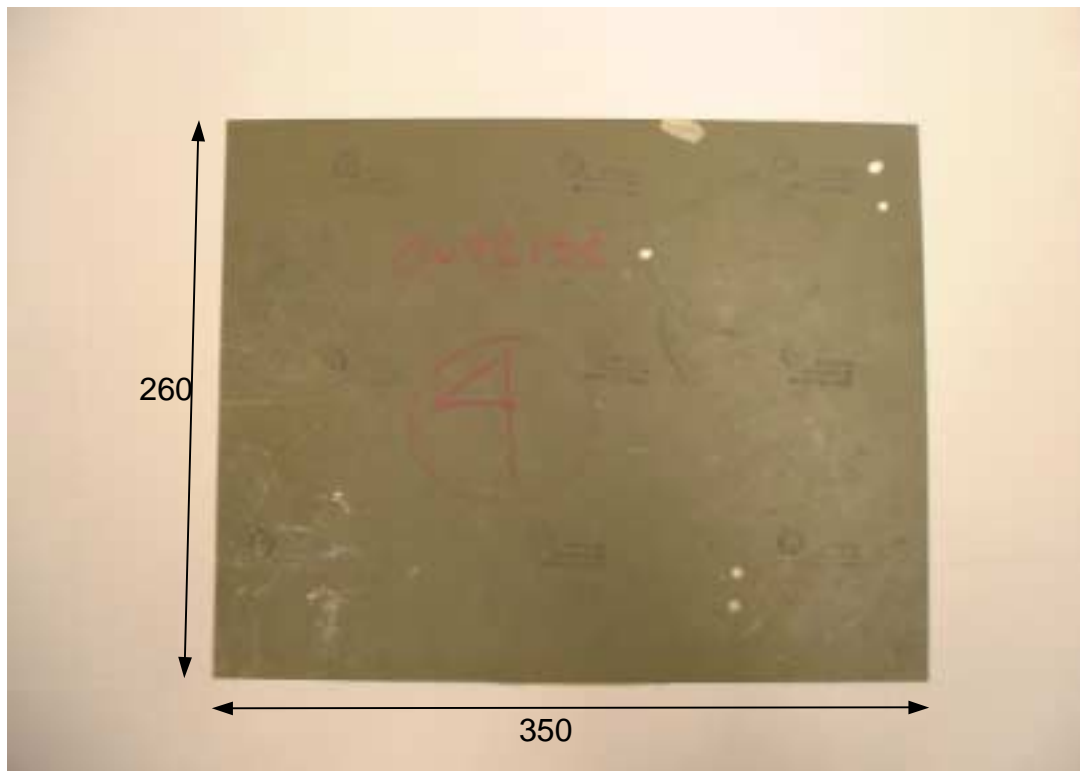
Figure 9. Sample # 4. Skin sample, no flaws.
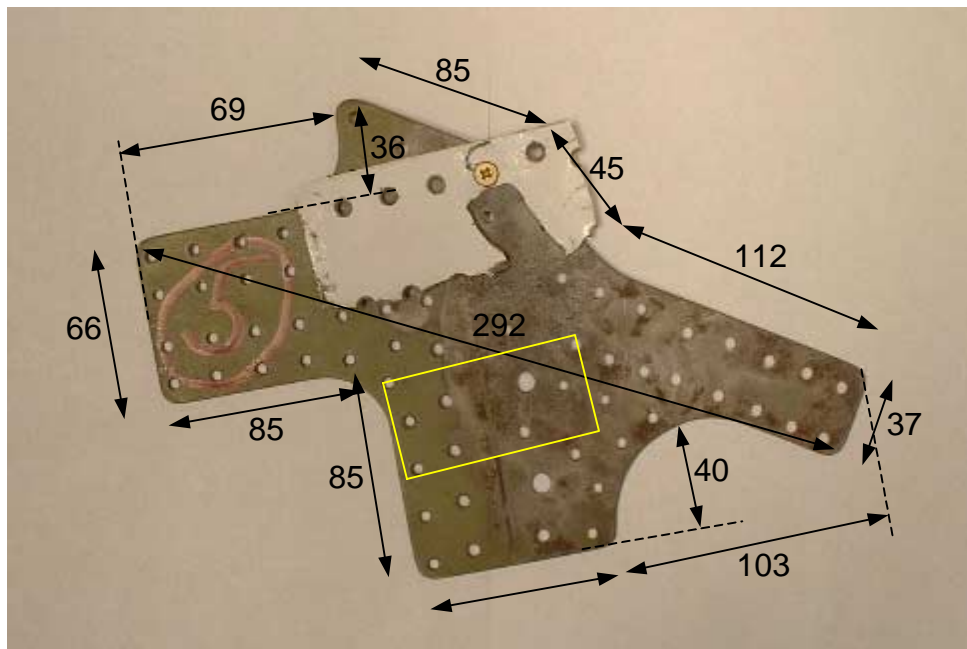
Figure 10. Sample # 5. Corrosion sample; corrosion between skin and frame member.

(numbers give dimensions in mm)
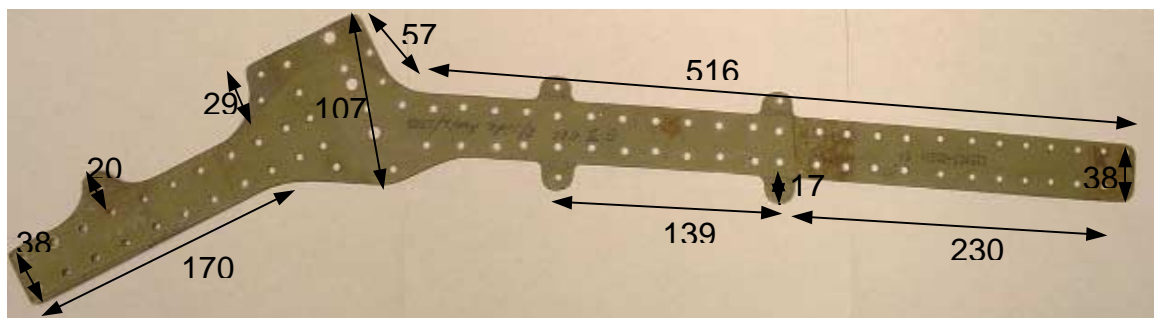
Figure 11. Sample # 6. Corrosion sample; corrosion between skin and frame member.
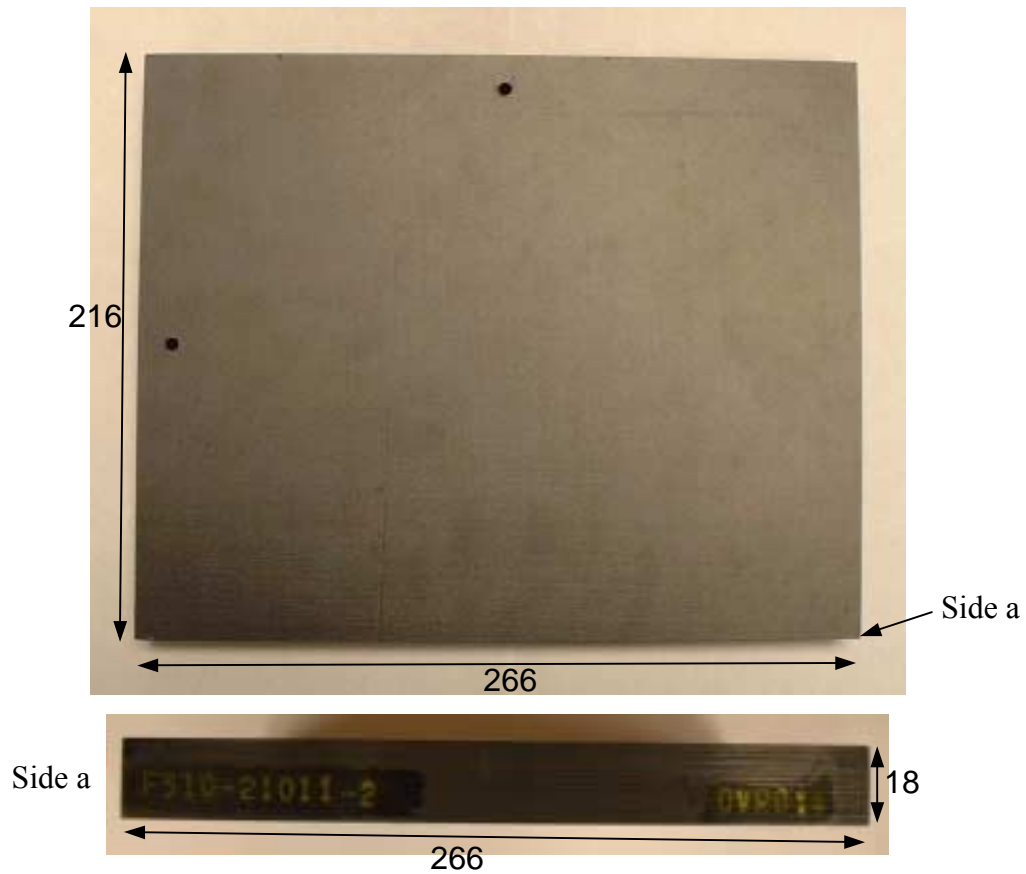
Figure 12. Sample #7. Boeing composite sample piece.

(numbers give dimensions in mm)
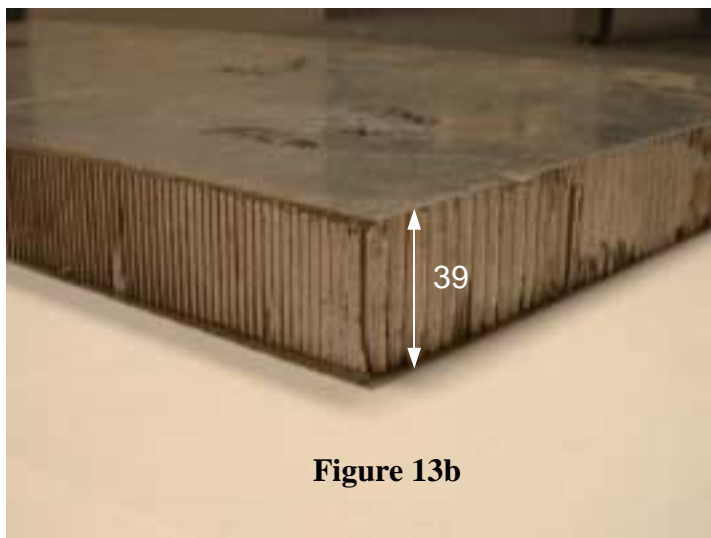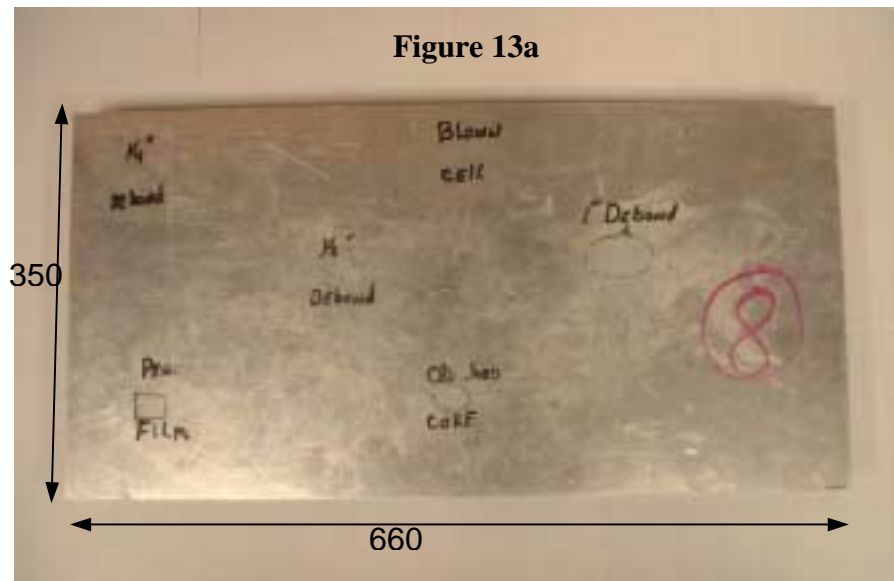
Figure 13a

Figure 13. Sample # 8. Aluminum honeycomb panel.
Figure 13a: view from top.
Figure 13b: view from side.

(numbers give dimensions in mm)
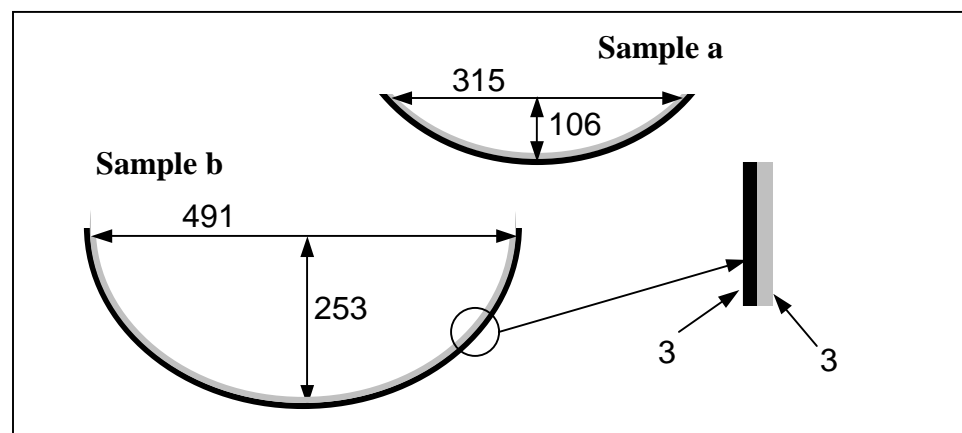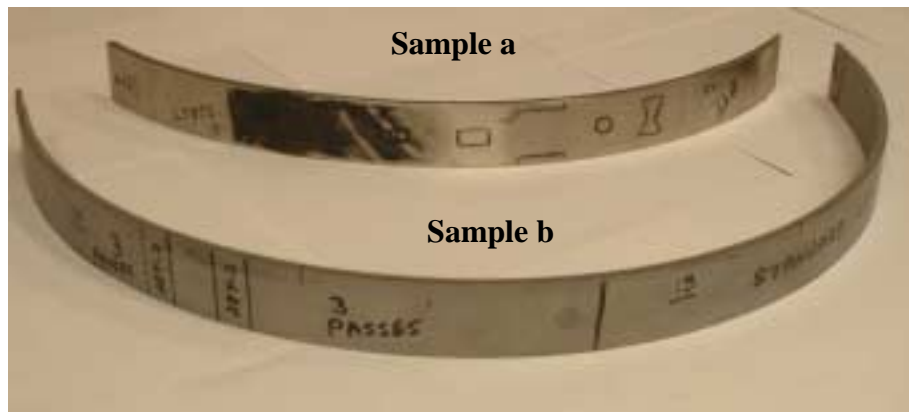
Figure 13b

Figure 14. Pratt and Whitney turbine blade casing pieces with defects.

(numbers give dimensions in mm)
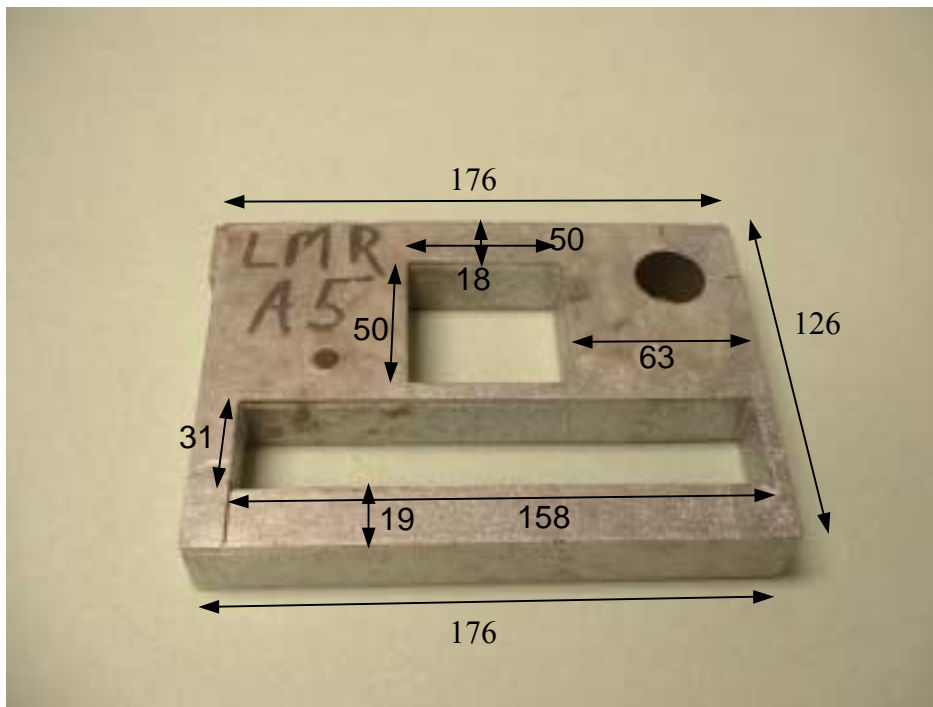
Figure 15. General Motors cast aluminum piece.

(numbers give dimensions in mm)
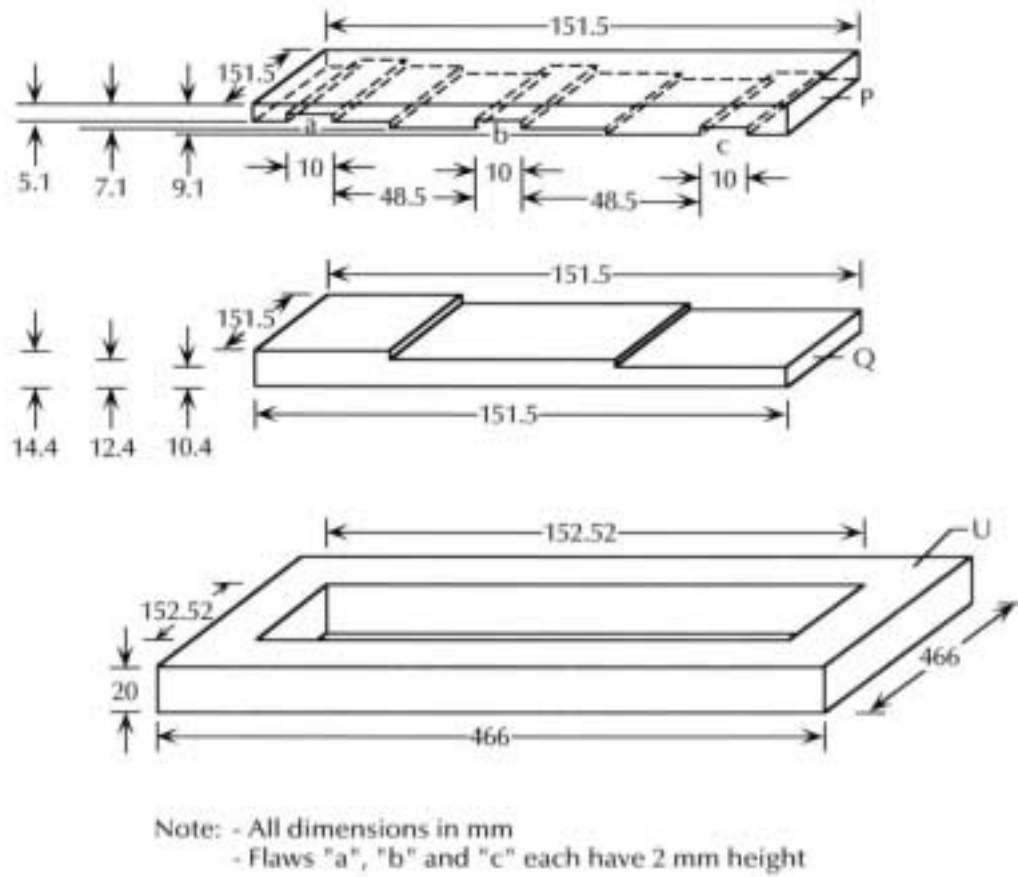
Figure 16. Schematic of machined aluminum flaw plate #1 with three flaws and aluminum frame.

SIDE VIEW OF TOP PLATE

SIDE VIEW OF BOTTOM PLATE

Note: All dimensions in mm
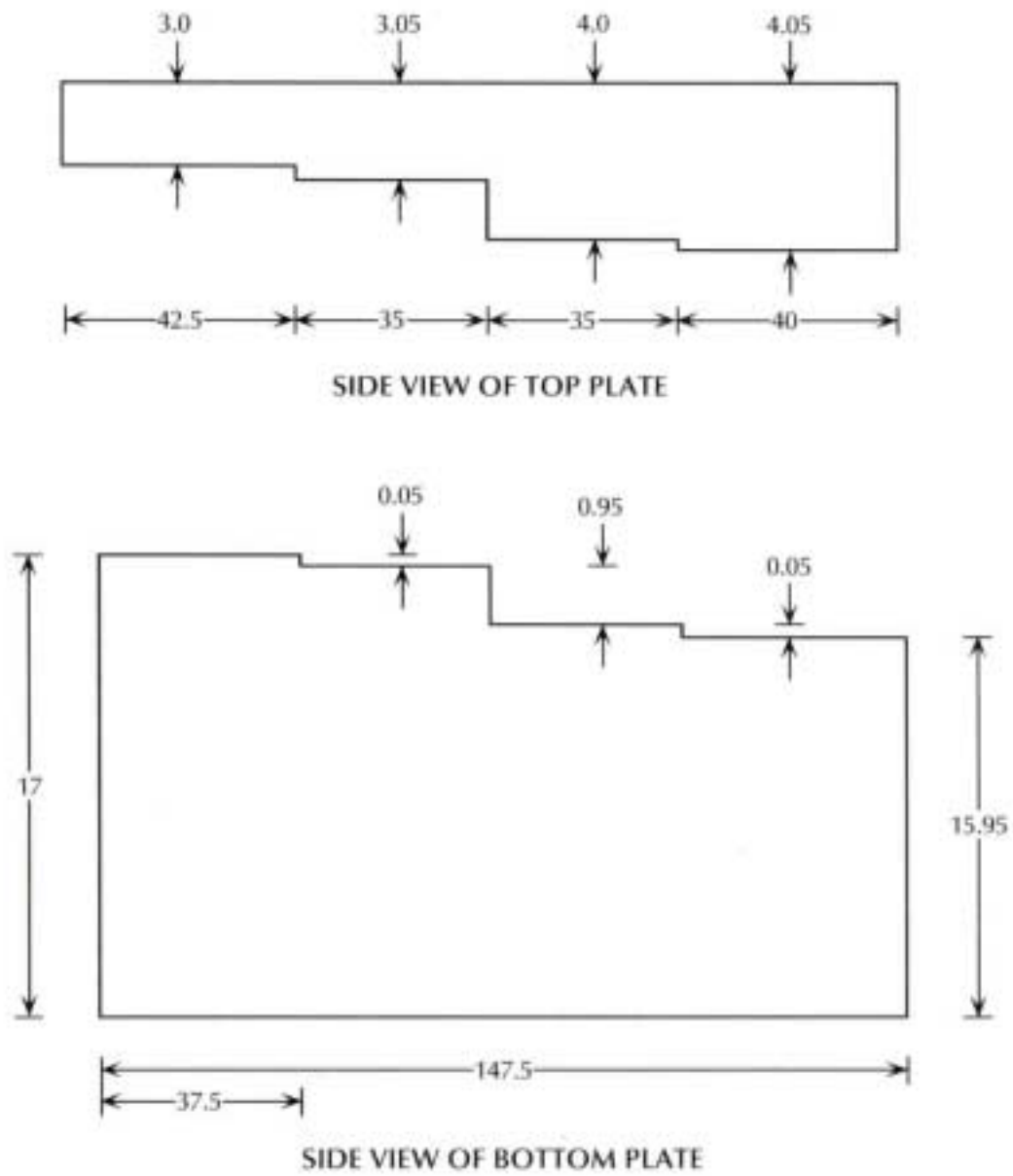
Figure 17. Schematic of machined aluminum flaw plate #2.

BOTTOM VIEW OF TOP PLATE

152.5

152.5

5→| |← 3→| |← 1→||← →| |←5 →| |←3 →||←1

SIDE VIEW OF TOP PLATE

0.5

0.3 3

|←16.5→| |←—20—→| |←—20—→||←—21—→| |←—21—→| |←—20—→||←16→|

Note: All dimensions in mm
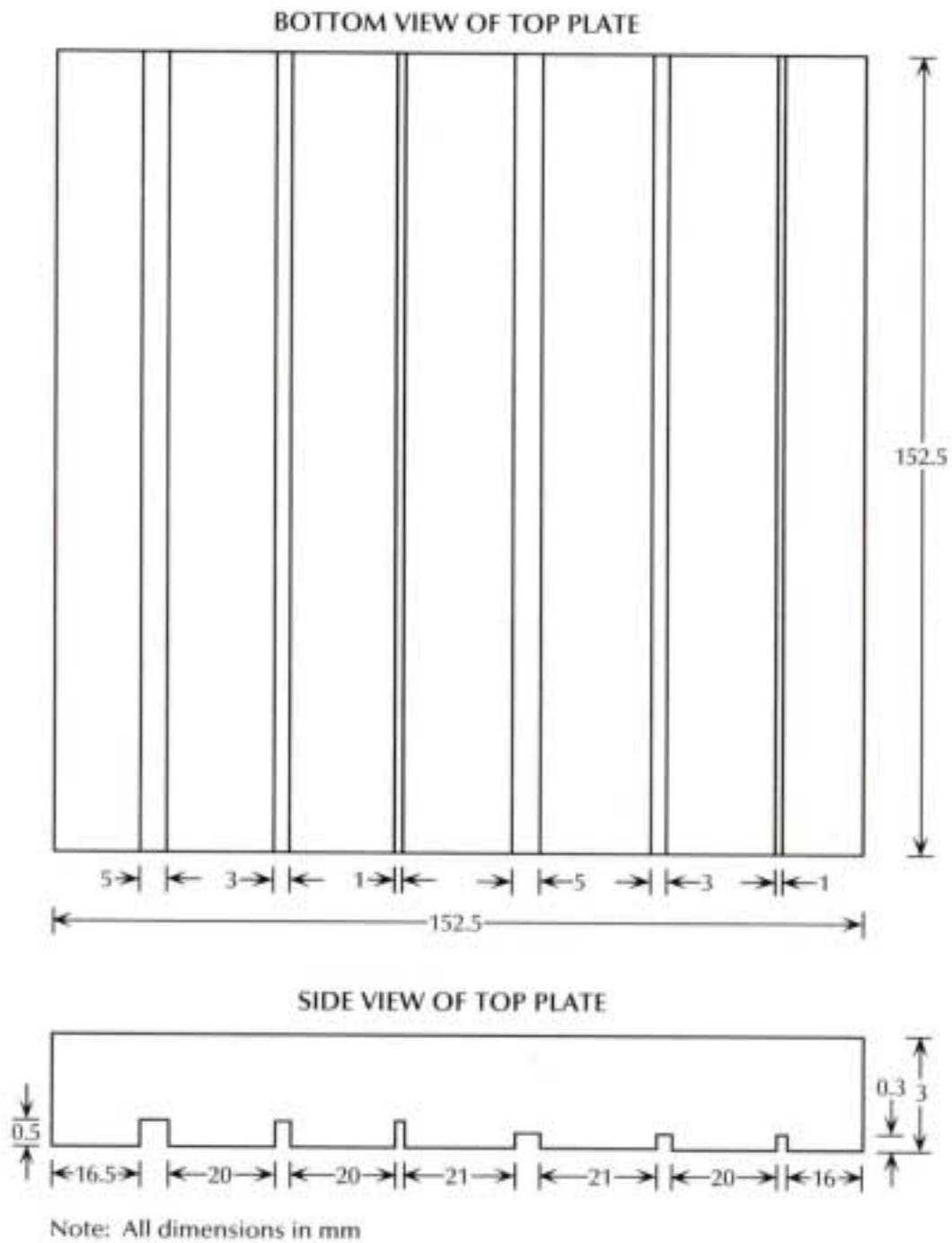
Figure 18. Schematic of top piece of machined aluminum flaw plate #3 with six flaws.

TOP AND BOTTOM VIEW OF BOTTOM PLATE

152.5

152.5

SIDE VIEW OF BOTTOM PLATE

17

Note: All dimensions in mm
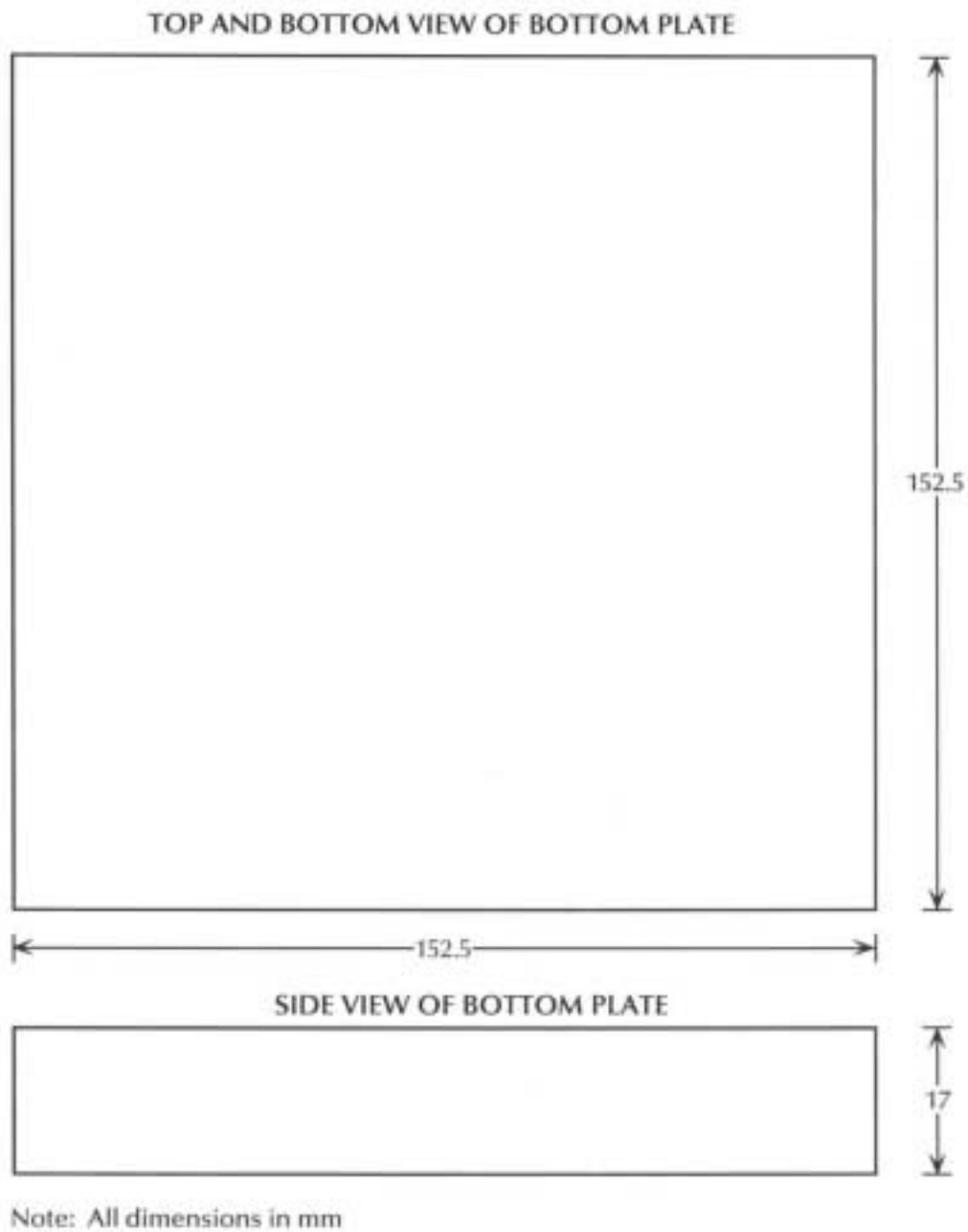
Figure 19. Schematic of bottom piece of machined aluminum flaw plate #3
with six flaws.
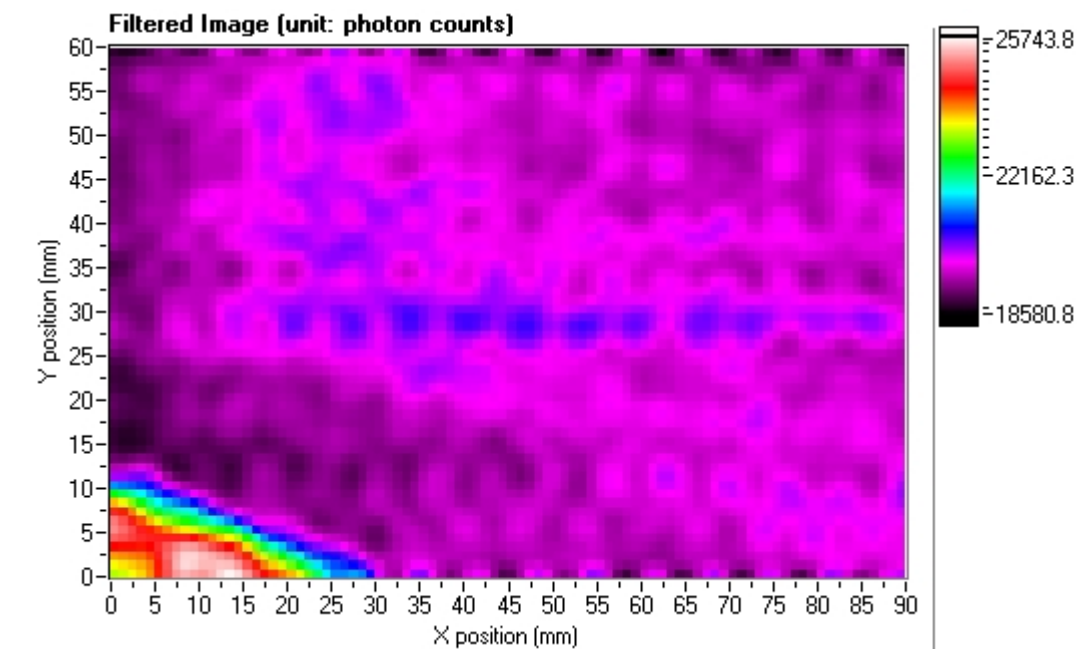
Figure 20.   Scan of Sample #1 at Location 3 with labeled side down.
(2 mm X-ray beam spot; 60 kVp and 5.7 mA; detector 2)
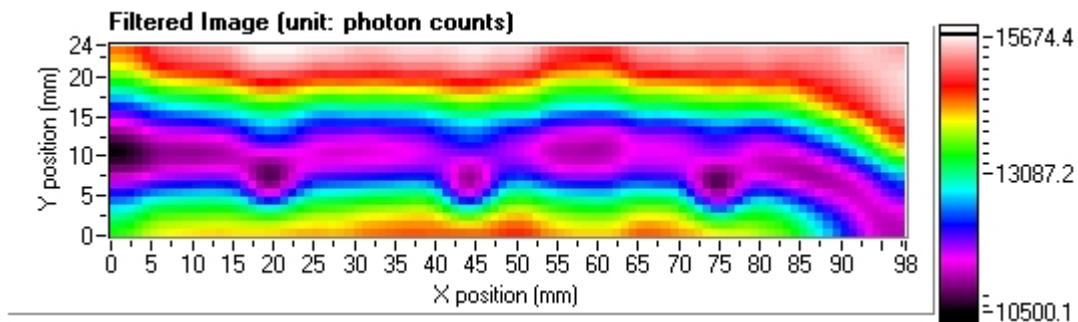
Figure 21. Scan of Sample #1 at Location 6 with labeled side up.
(2 mm X-ray beam spot; 50 kVp and 5.5 mA; detector 1)

Figure 22. Scanned Areas for Sample #2.
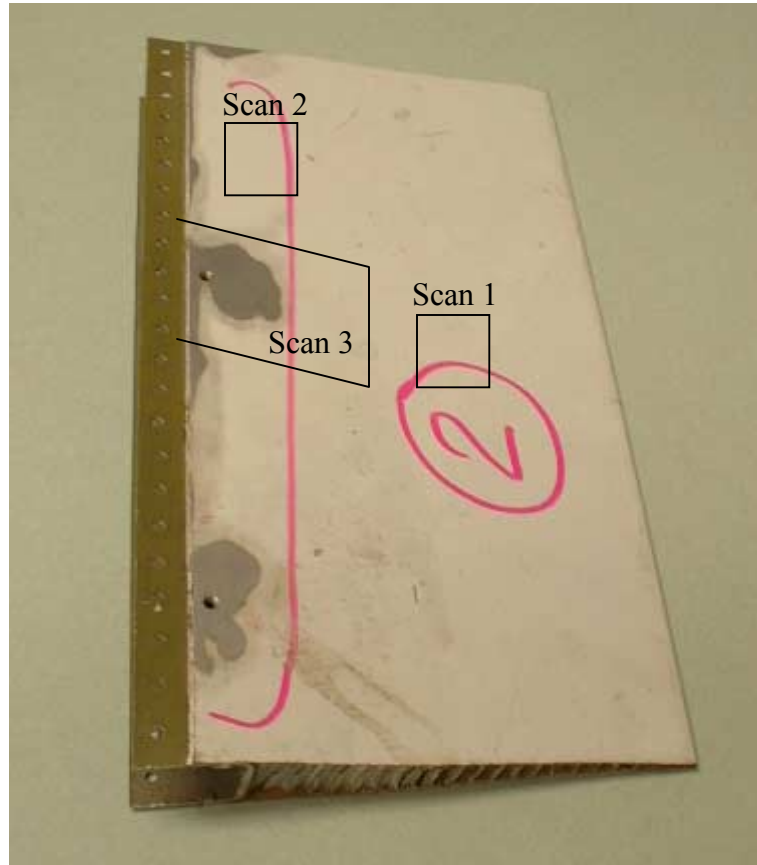
Scan 1

# of z level 1
# of y pixels 20
# of x pixels 20
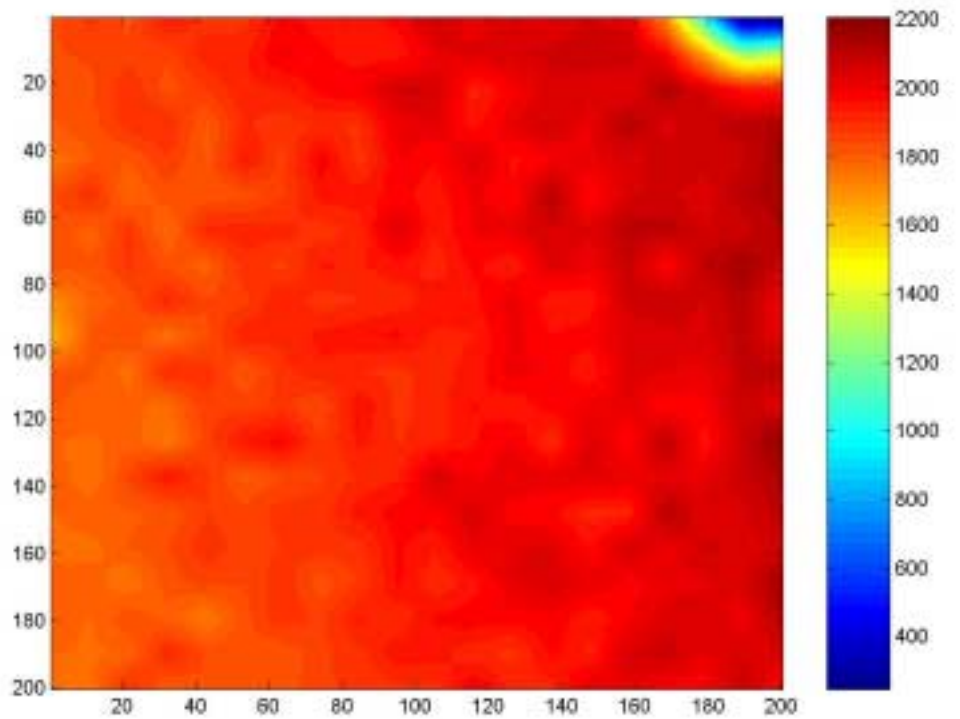pixel scan time 0.5 s

pixel size 1 mm
75 kv and 9 ma
800 Volts
lld 0.4 window 9.6
beam hole 2 mm
z=75 mm (-10)
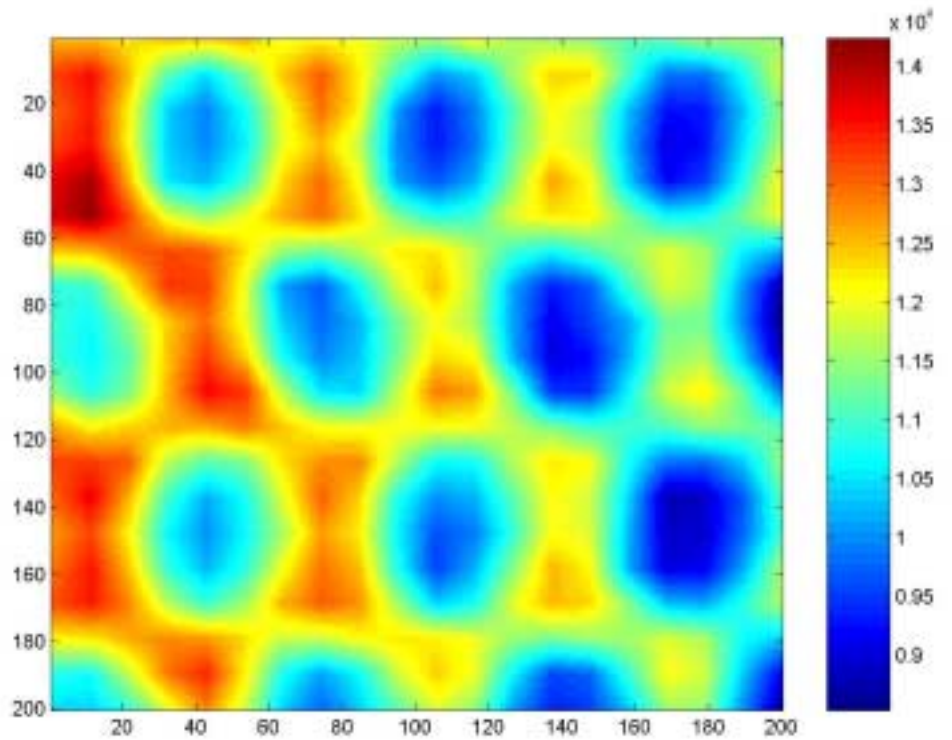
Scan 2

# of z level 1
# of y pixels 20
# of x pixels 20
pixel scan time 0.5 s

pixel size 1 mm
75 kv and 9 ma
800 Volts
lld 0.4 window 9.6
beam hole 2 mm
z=80 mm (-5)
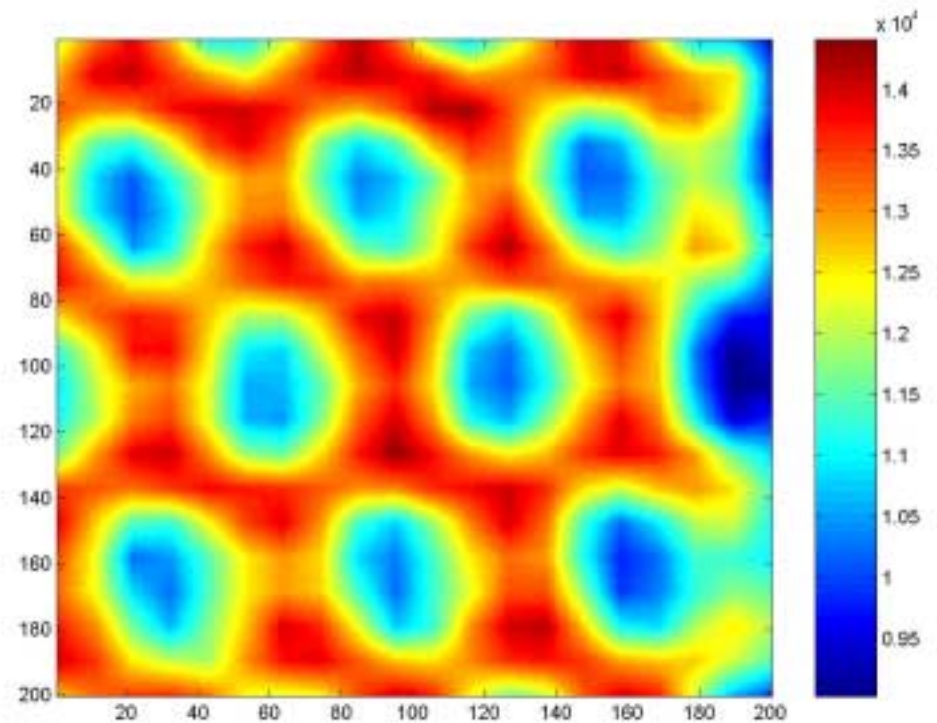
Figure 23.   Scan 1 and Scan 2 for Sample # 2.
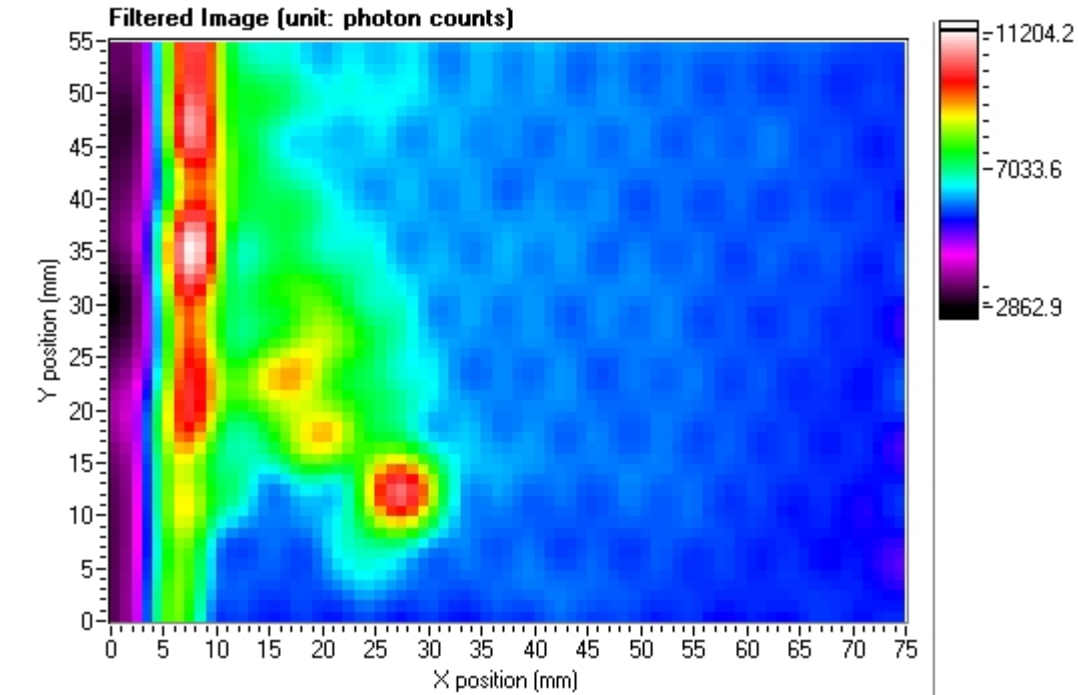
Figure 24. Scan 3 for Sample #2 with labeled side up.

(2 mm X-ray beam spot; 55 kVp and 5 mA; detector 1)

red vertical strip at about x = 7 is corrosion
red spot centered at x = 27 and y = 12 is a cell with water
green area is a region of crushed core
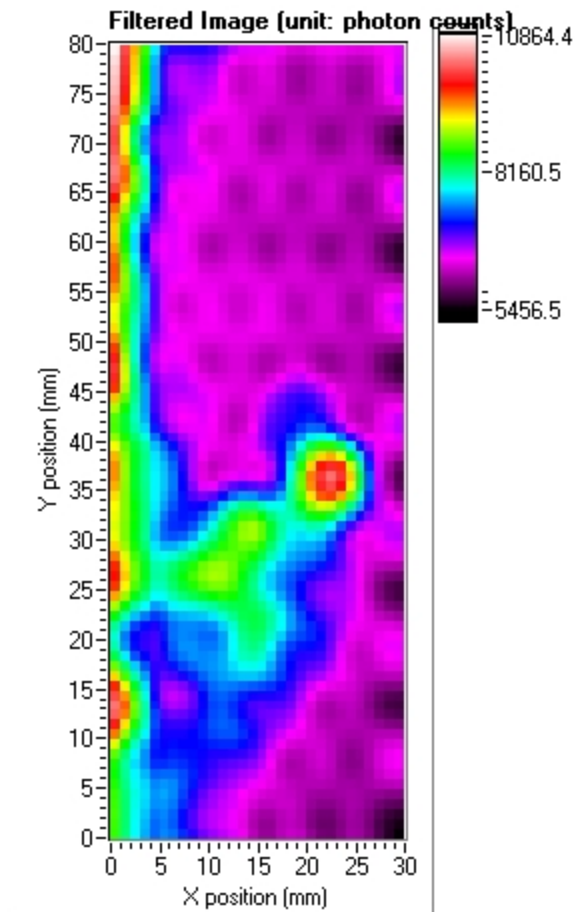
Figure 25. Scan 3 for Sample #2 with labeled side down.

(2 mm X-ray beam spot; 55 kVp and 5 mA; detector 1)

red vertical strip at about x = 0 is corrosion
red spot centered at x = 22 and y = 36 is a cell with water
green area is a region of crushed core
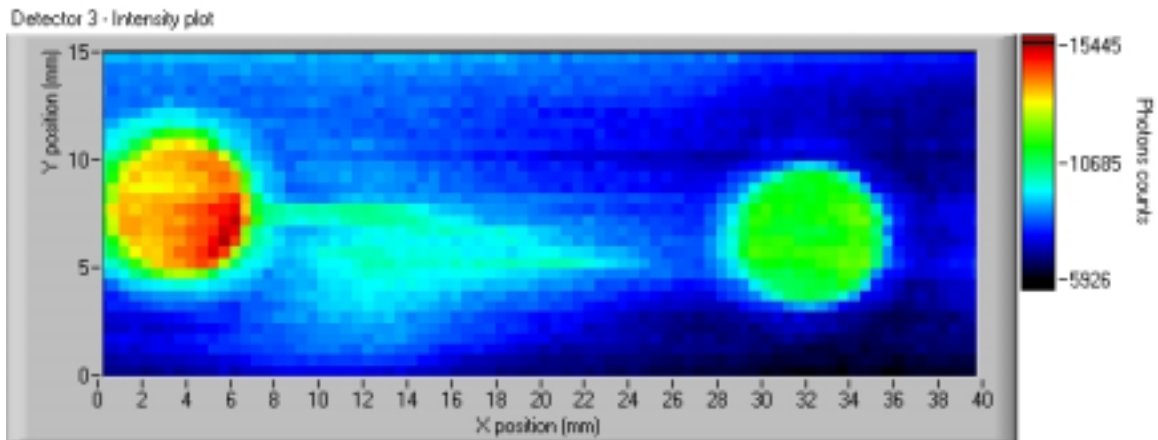
Figure 26a. **Scan of Sample #3 – unprocessed image with no aluminum skin covering; scanned area marked by the blue lines in Figure 26b.**

(1 mm X-ray beam spot; 70 kVp and 8 mA; detector 3)
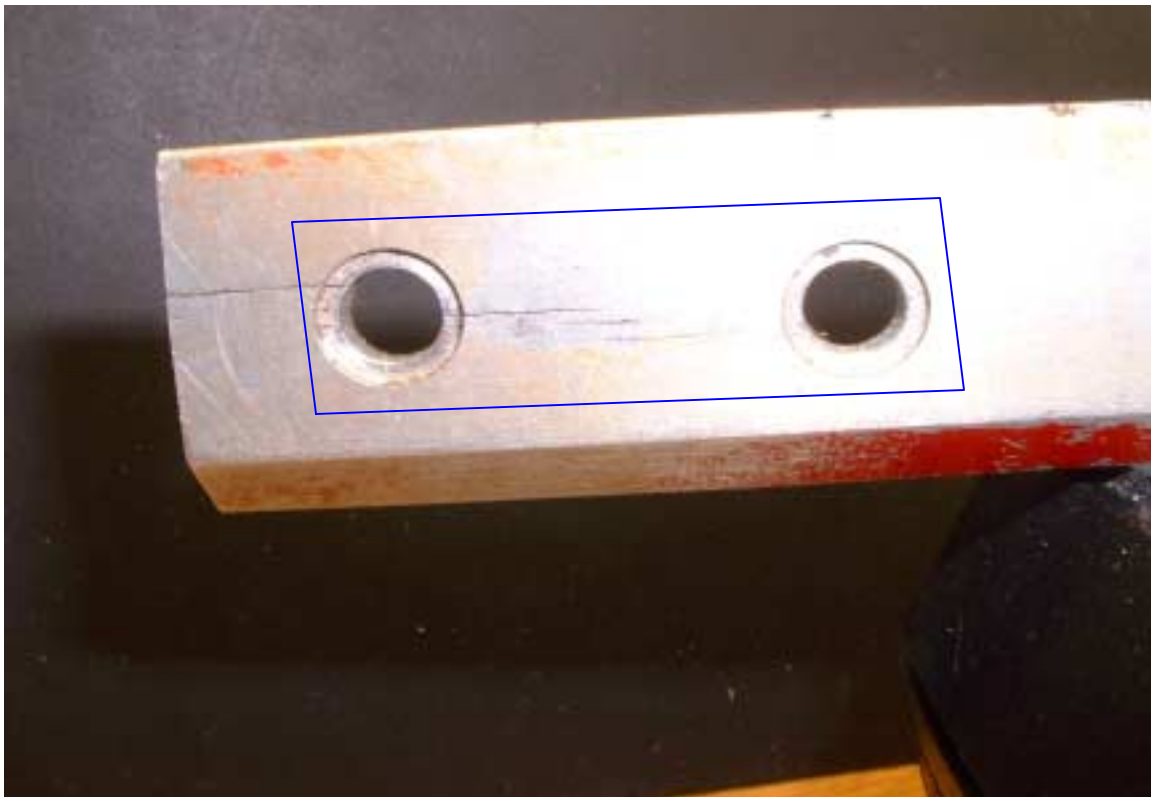
Figure 26b. **Photograph showing cracks around fastener hole of Sample #3 – magnification about 2x actual size.**
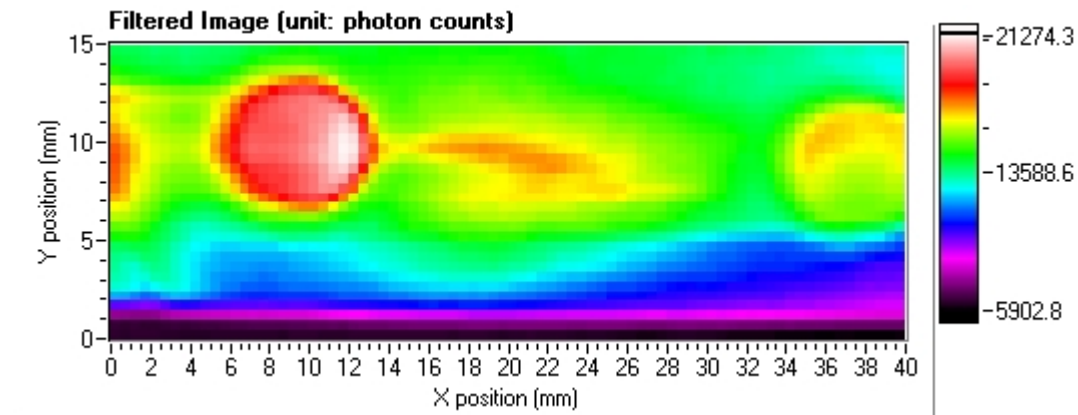
Figure 27. **Scan of Sample #3 – processed image with no aluminum skin covering; scanned area marked by the blue lines in Figure 8.**

(1 mm X-ray beam spot; 75 kVp and 8 mA; detector 3)

[The detector collimator length and x-ray generator voltage setting used here are the same as those used to image sample 3 with an aluminum skin covering in Figure 28.]

.
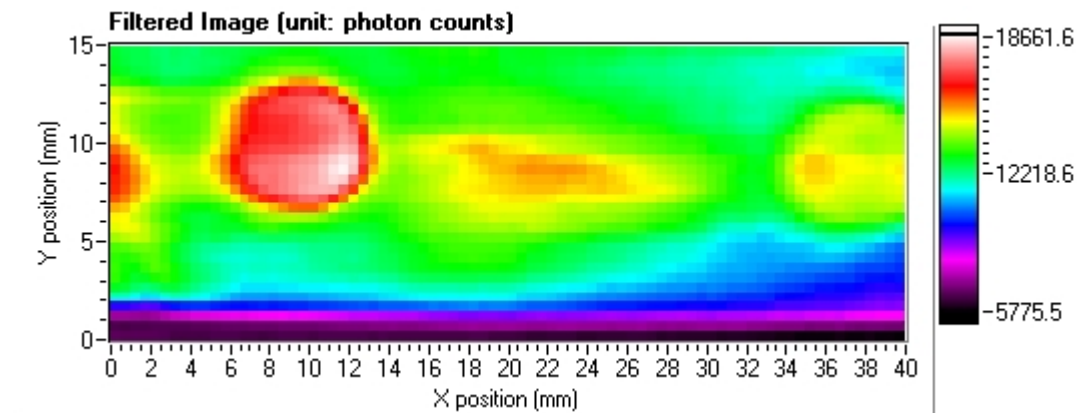
Figure 28. **Scan of Sample #3 – processed image with the sample covered by aluminum skin; scanned area marked by the blue lines in Figure 8.**

(1 mm X-ray beam spot; 75 kVp and 8 mA; detector 3)

[Relative to the previous image, which was taken without an aluminum skin covering, the number of counts (image intensity) is lower.]

Figure 29.   Scanned Areas and Scan 1 for Sample # 5.
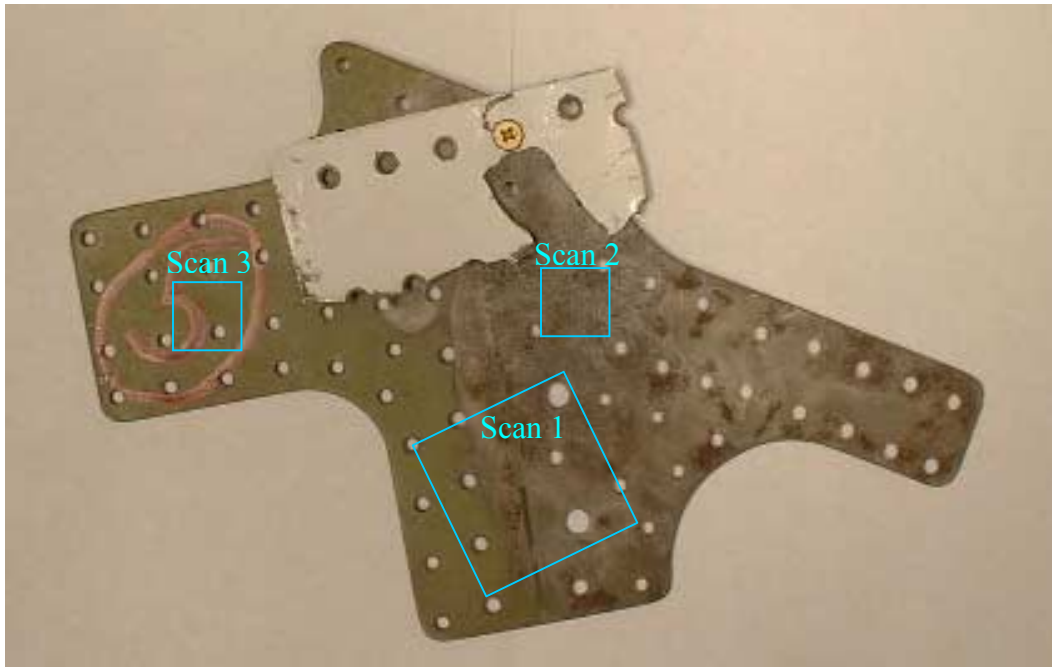
Scan 1

# of z level 1
# of y pixels 50
# of x pixels 50
pixel scan time 0.5 s

pixel size 1 mm
75 kv and 9 ma
800 Volts
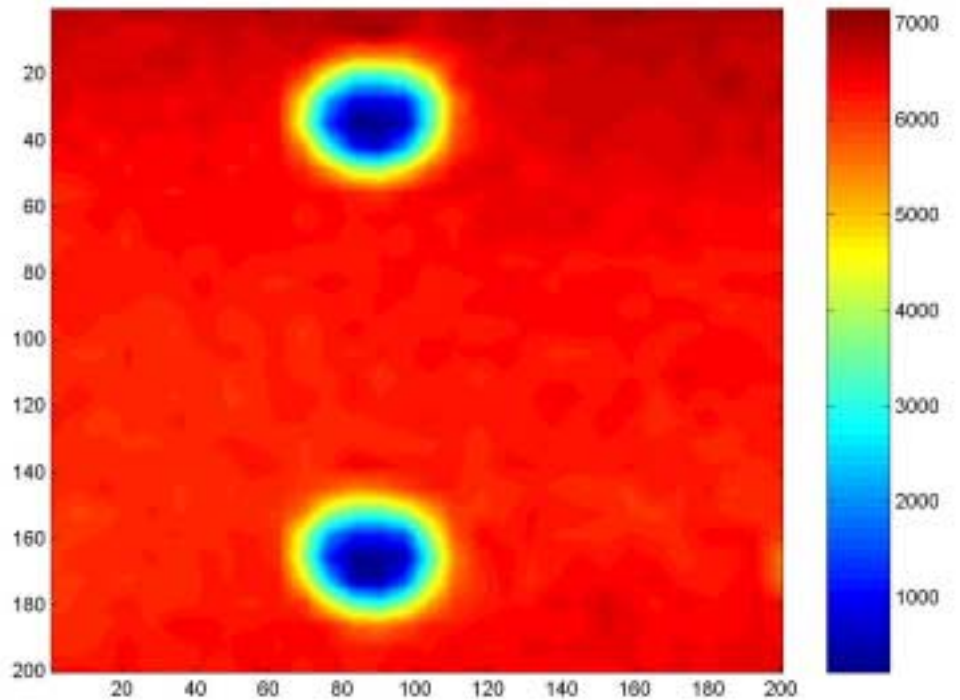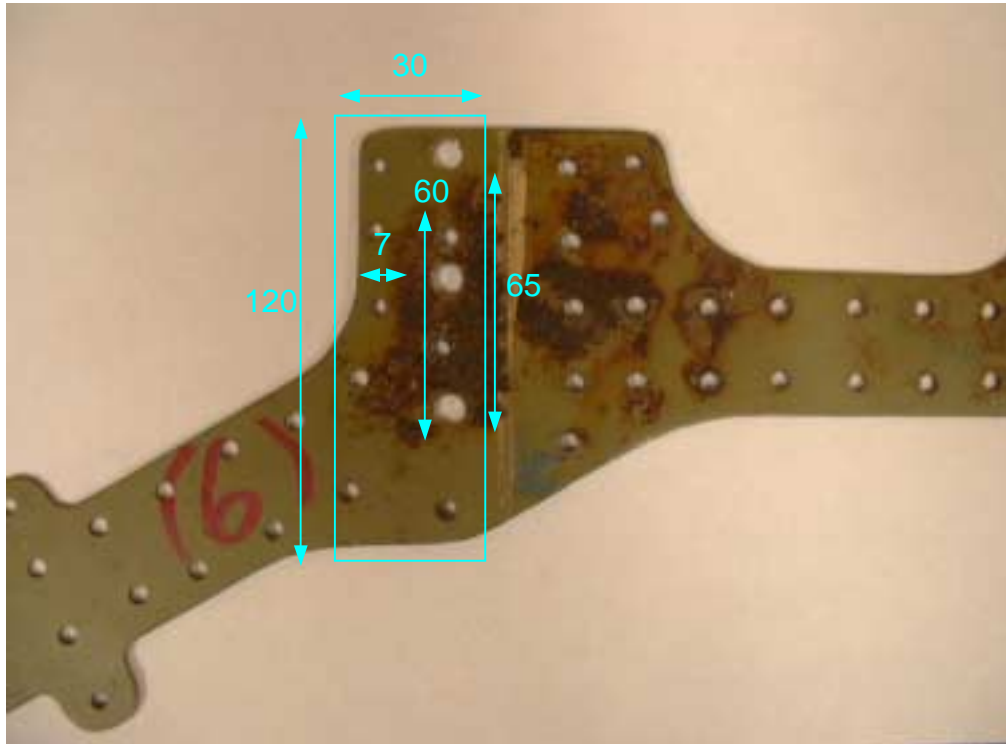lld 0.4 window 9.6
beam hole 2 mm
z=72 mm(-13)
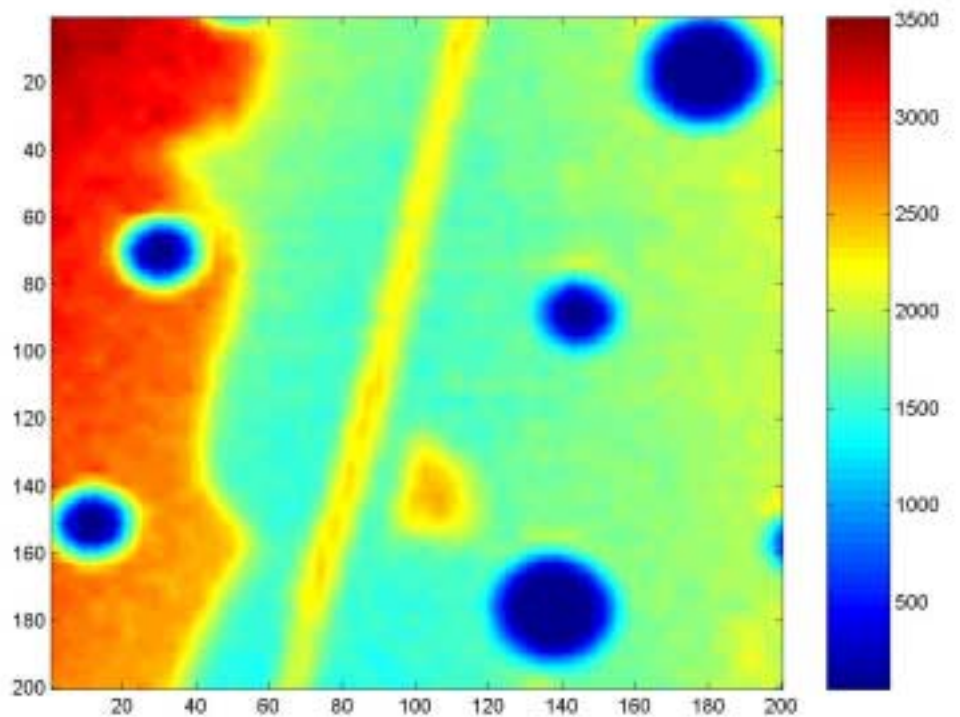
Scan 2

# of z level 1
# of y pixels 20
# of x pixels 20
pixel scan time 0.5 s

pixel size 1 mm
75 kv and 9 ma
800 Volts
lld 0.4 window 9.6
beam hole 2 mm
z=72 mm (-13)

Scan 3

# of z level 1
# of y pixels 20
# of x pixels 20
pixel scan time 0.5 s

pixel size 1 mm
75 kv and 9 ma
800 Volts
lld 0.4 window 9.6
beam hole 2 mm
z=72 mm (-13)
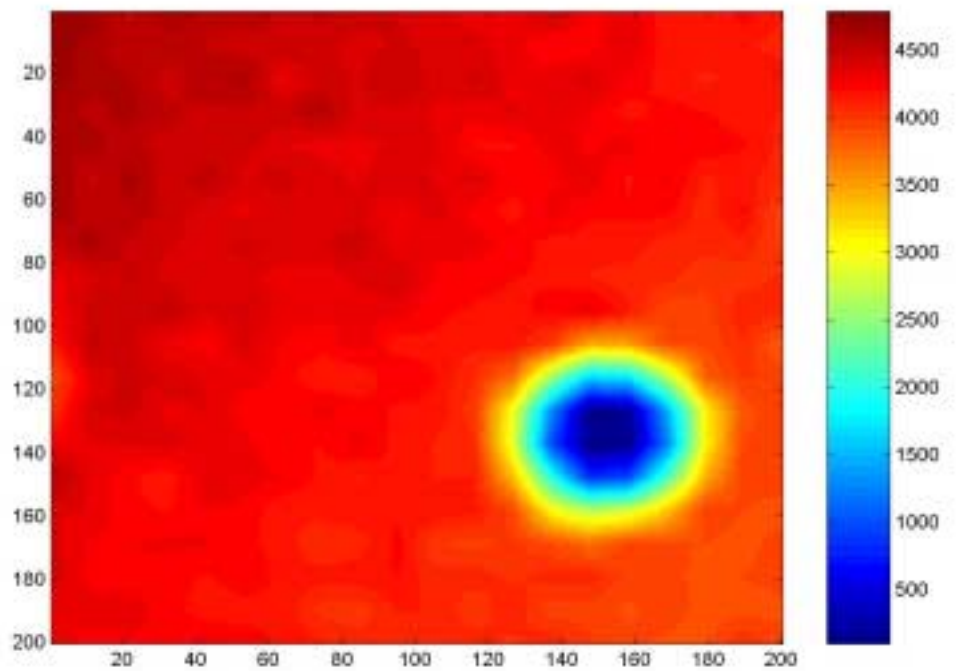
Figure 30.   Scan 2 and Scan 3 for Sample # 5.
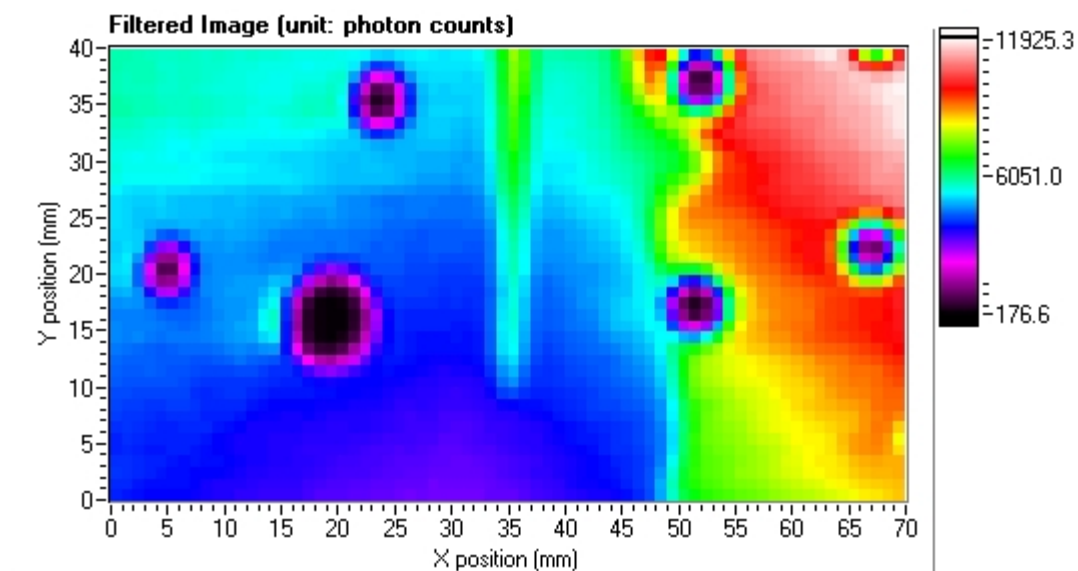
Figure 31. Scan of Sample #5 with labeled side up – scanned area marked by the yellow lines in Figure 10.

(2 mm X-ray beam spot; 75 kVp and 8.5 mA; detector 3)

[corroded area has lower intensity (green and blue) than uncorroded areas]

Figure 32. Scanned Areas for Sample # 6.
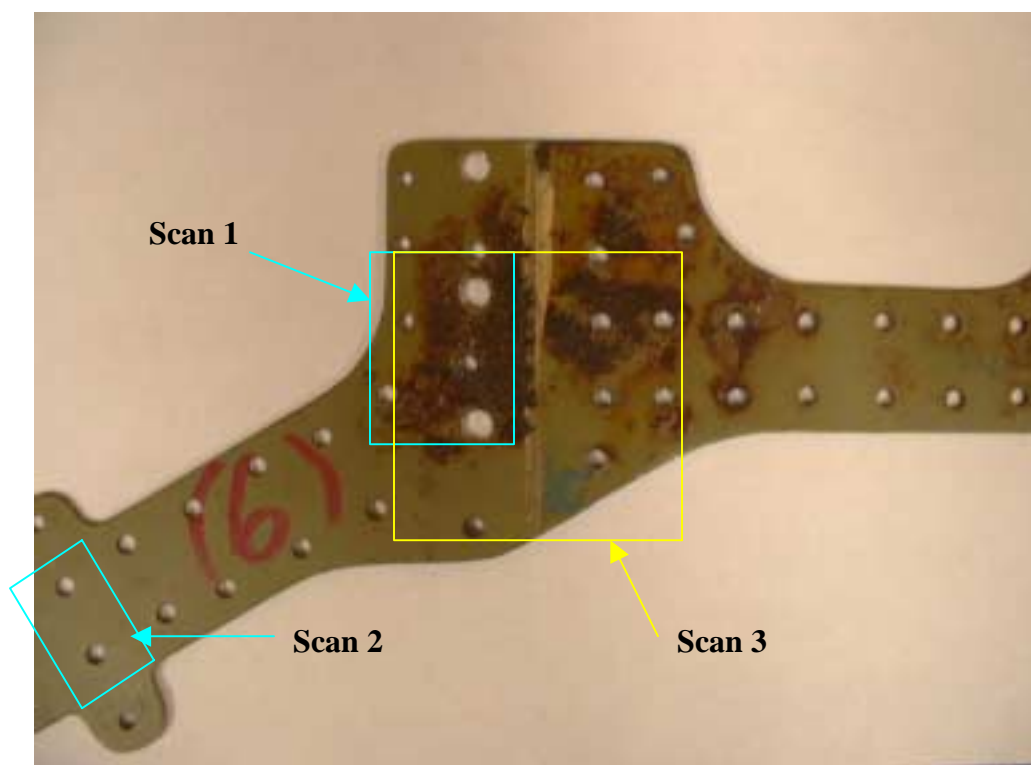
Scan 1

# of z level 1
# of y pixels 50
# of x pixels 50
pixel scan time 0.5 s

pixel size 1 mm
75 kv and 9 ma
800 Volts
lld 0.4 window 9.6
beam hole 2 mm
z=65 mm (-20)
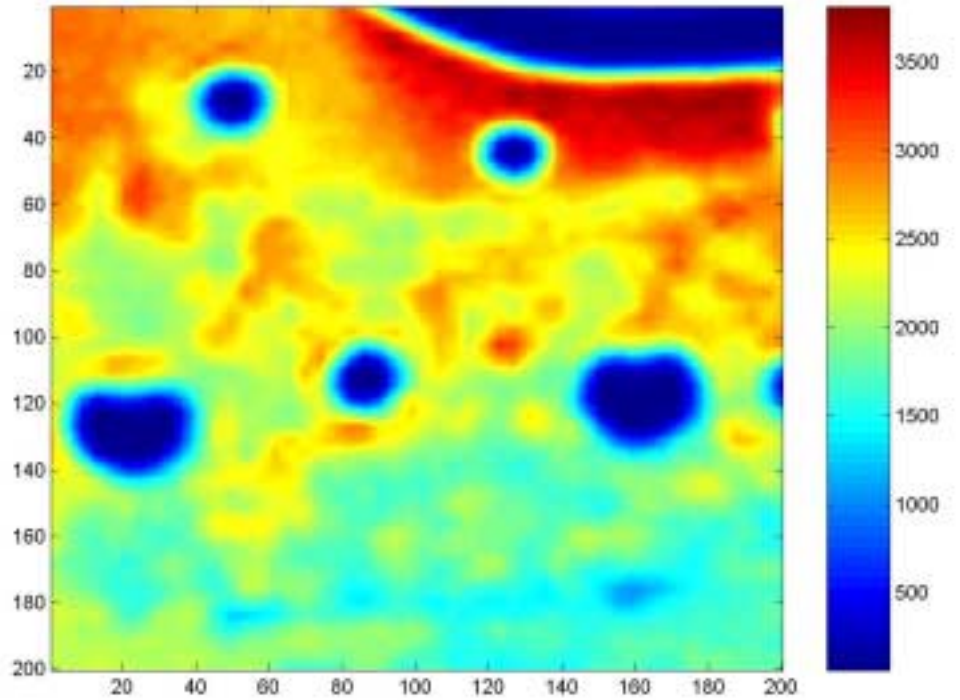
Scan 2

# of z level 1
# of y pixels 30
# of x pixels 30
pixel scan time 0.5 s

pixel size 1 mm
75 kv and 9 ma
800 Volts
lld 0.4 window 9.6
beam hole 2 mm
z=65 mm(-20)

Figure 33.   Scan 1 and Scan 2 for Sample # 6.

Figure 34.   Reverse Side Scan of Sample # 6.

Sample #6 Image with labeled side facing down.

Settings
x-ray generator: 75kv 9ma
detectors HV: 800V
lld 0.4 window 9.6
beam hole 2mm

z=65 mm (-20)

# of z level: 1
# of y pixels: 20
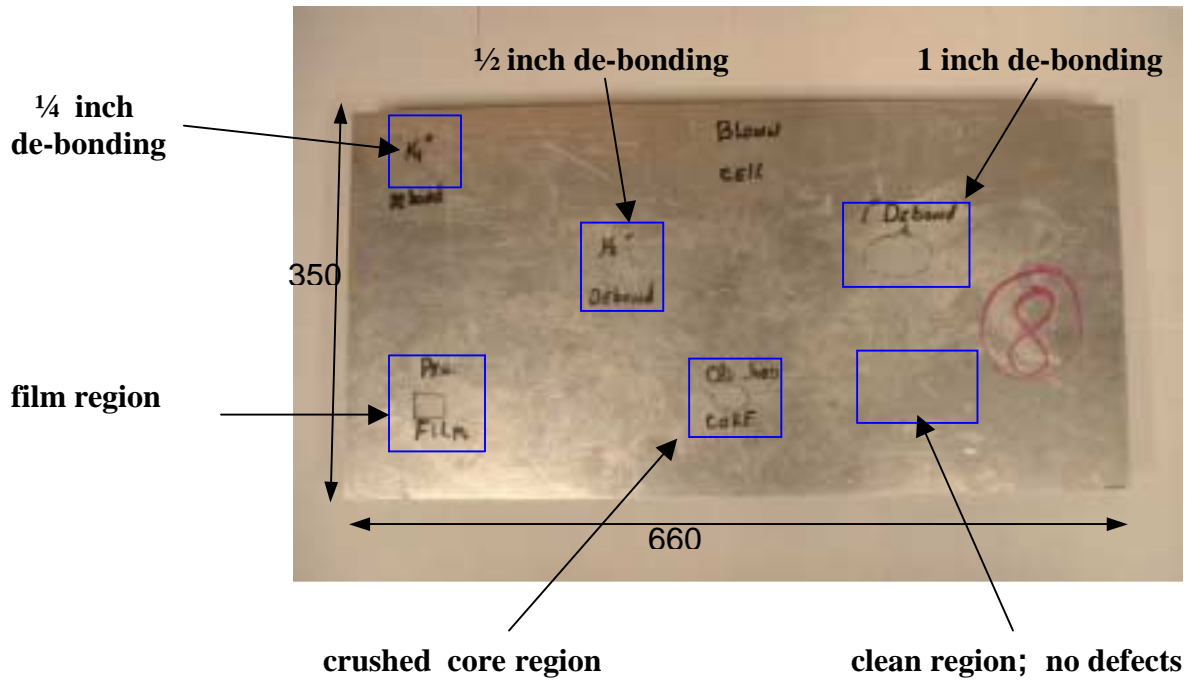# of x pixels: 60
scan time: 2 s
pixel size: 2 mm
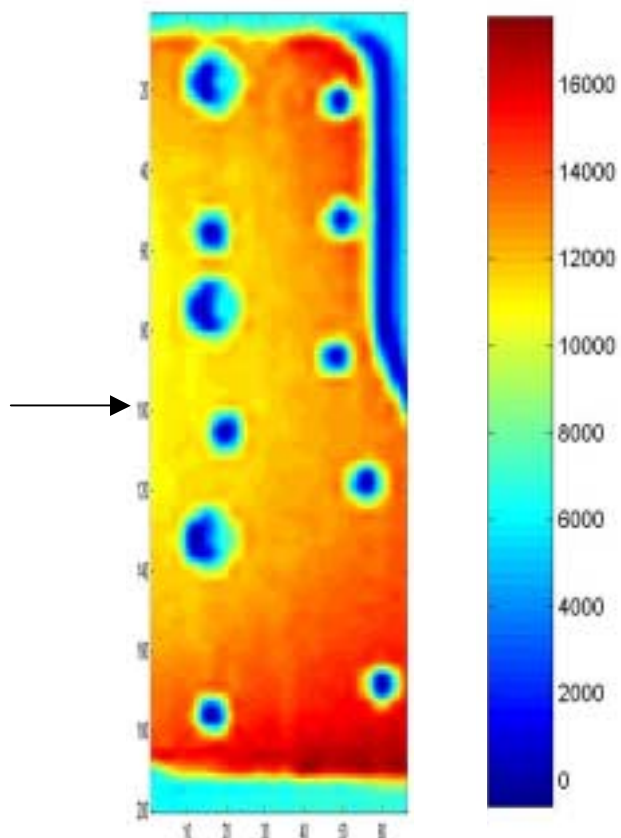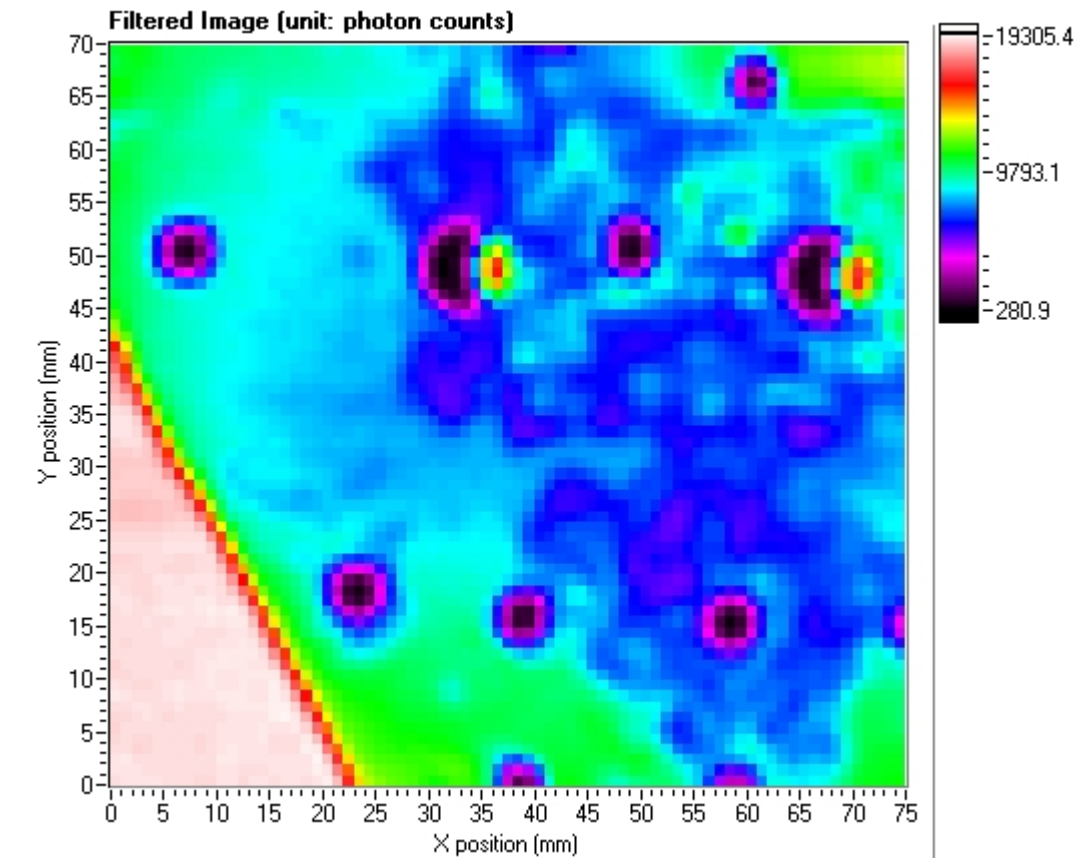
Figure 35.   Scan of Sample #6 with labeled side up – scan area marked by yellow lines in Figure 32.

(2 mm X-ray beam spot; 75 kVp and 8.5 mA; detector 2)

[The corroded area has lower intensity (dark blue) than uncorroded areas. The corroded region would show more sharply if the X-ray generator voltage were reduced slightly and/or if the detector colli-mator length was slightly reduced. Settings used in this scan were those that also allowed the corrosion to show well when the sample was scanned with the corroded side facing down.]
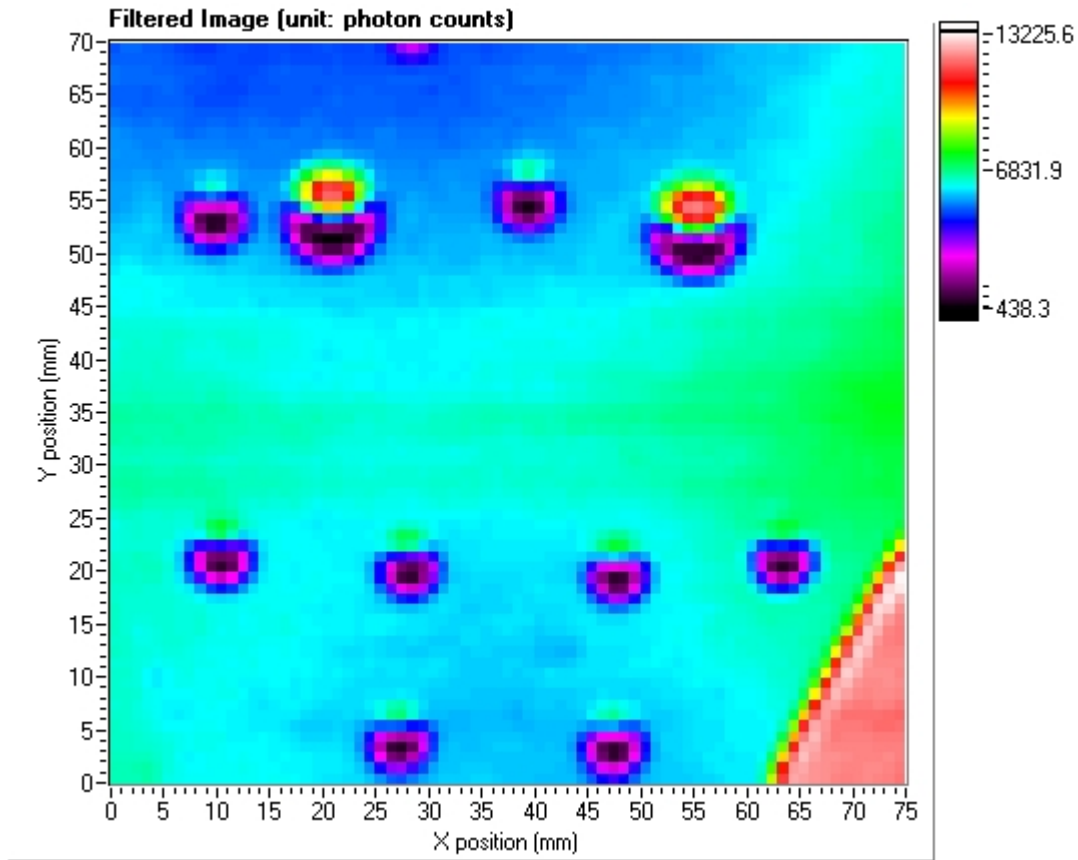
Figure 36. **Scan of Sample #6 with labeled side down – scan area marked by yellow lines in Figure 32.**

(2 mm X-ray beam spot; 75 kVp and 8.5 mA; detector 1)

[Corroded area has lower intensity (blue) than the uncorroded areas. Although this scan was taken with the clean side up, and the corroded side facing down, the corrosion is apparent, even through this 2 mm thick frame member.]

Figure 37. Scanned Areas and Scan 1 for Sample # 8.

¼ inch de-bonding

½ inch de-bonding

1 inch de-bonding

350

film region

660

crushed core region

clean region; no defects

Scan 1
1 inch diameter
debonding region

# of z level 1
# of y pixels 30
# of x pixels 40
pixel scan time 1 s

pixel size 1 mm
75 kv and 9 ma
800 Volts
lld 0.4 window 9.6
beam hole 2 mm
z=85 mm(0)
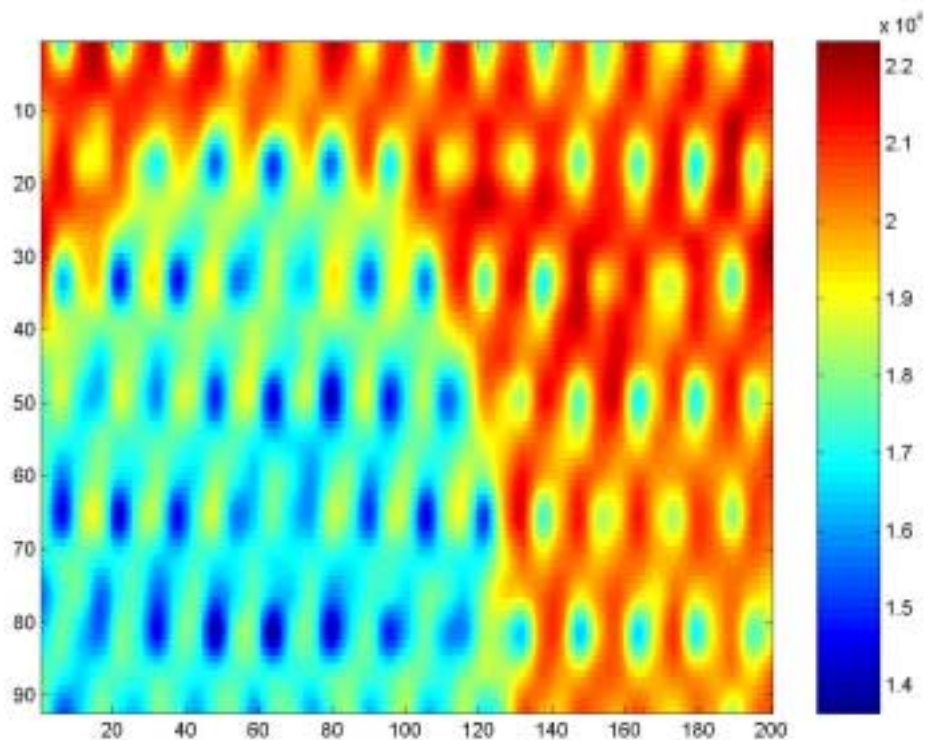
Scan 2
0.5 inch diameter
debonding region

# of z level 1
# of y pixels 30
# of x pixels 30
pixel scan time1 s

pixel size 1 mm
75 kv and 9 ma
800 Volts
lld 0.4 window 9.6
beam hole 2 mm
z=85 mm(0)
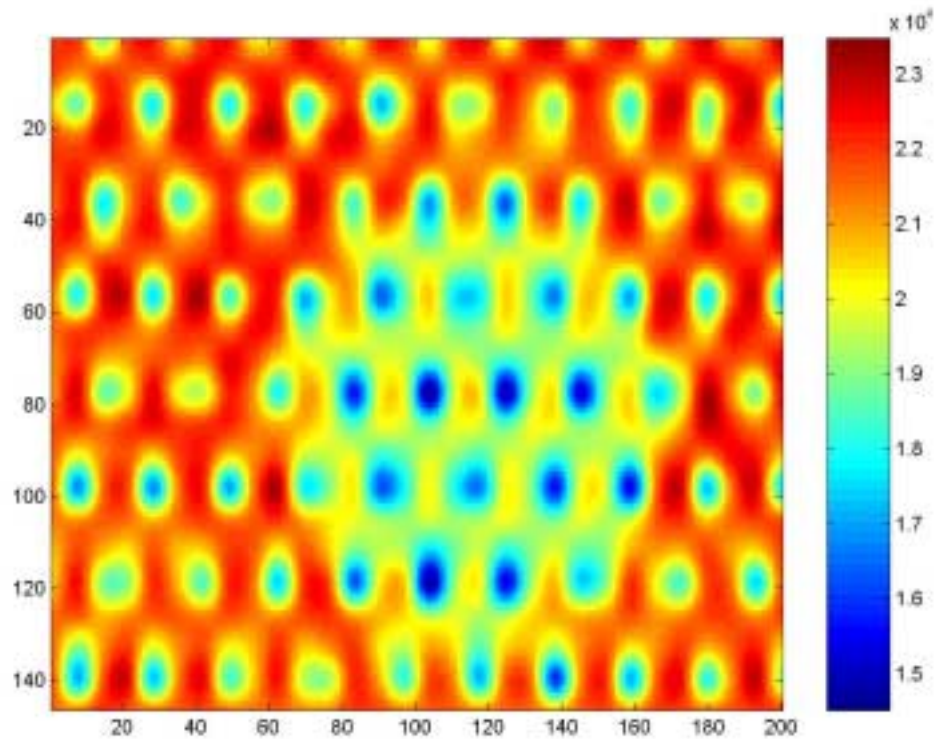
Scan 3
region with no
flaws or defects

# of z level 1
# of y pixels 20
# of x pixels 20
pixel scan time1 s

pixel size 1 mm
75 kv and 9 ma
800 Volts
lld 0.4 window 9.6
beam hole 2 mm
z=85 mm (0)
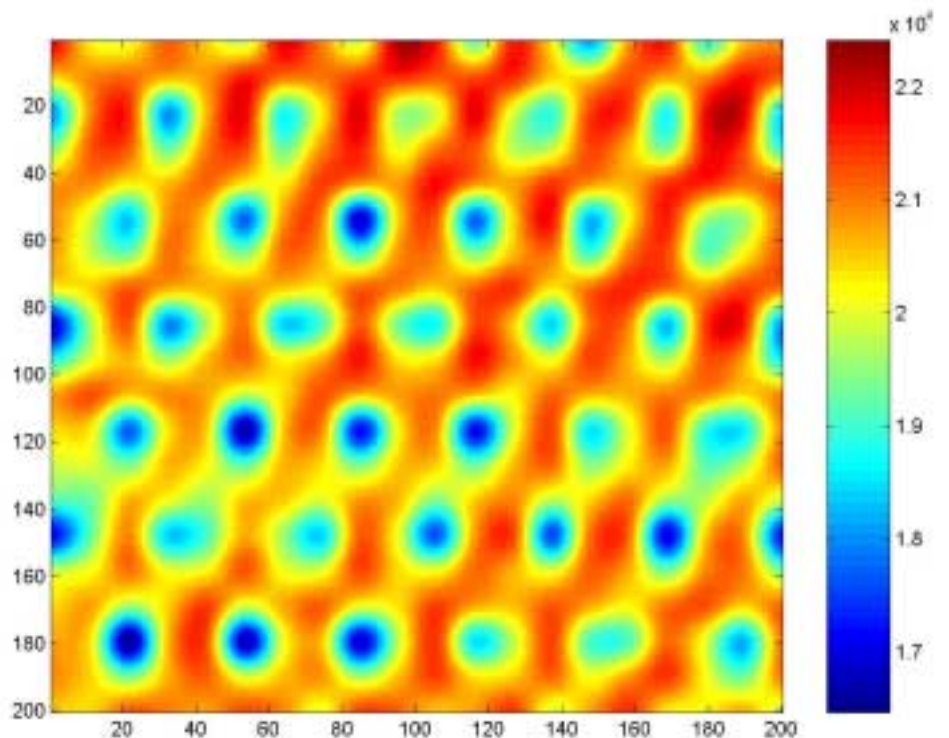
Figure 38. Scans 2 and 3 for Sample # 8.

53
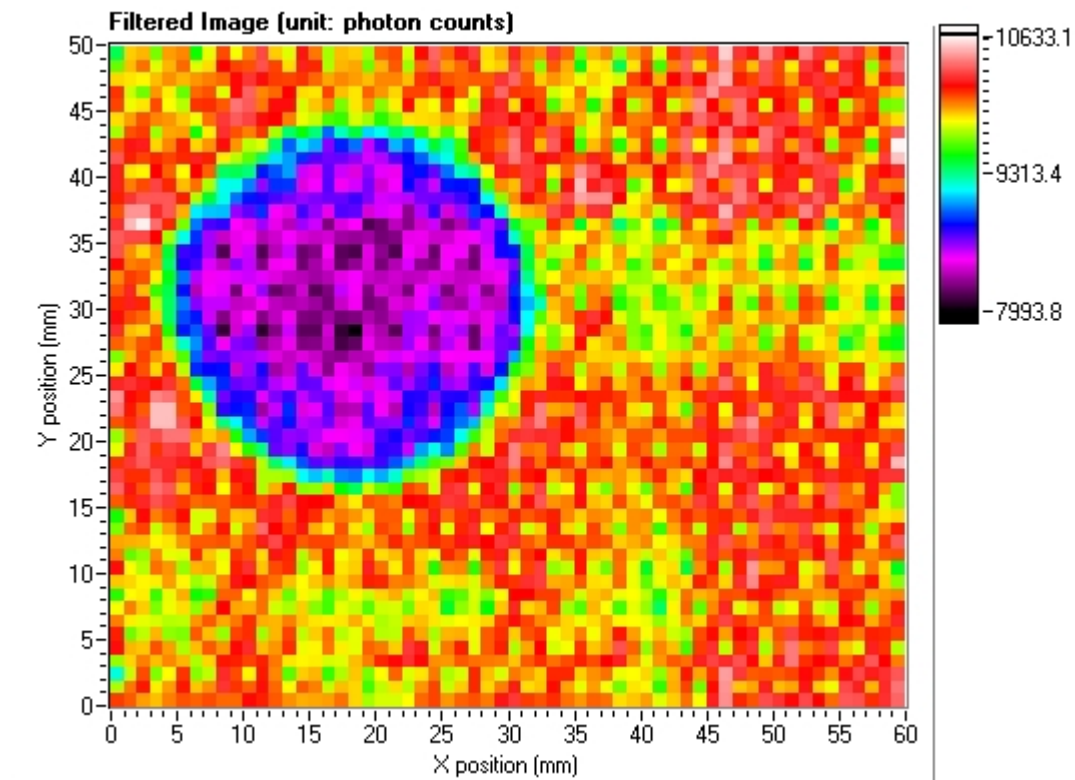
Figure 39. Scan of the 1 inch diameter debonding region of Sample #8 - labeled side facing up.

(2 mm X-ray beam spot; 70 kVp and 7.5 mA; detector 3)
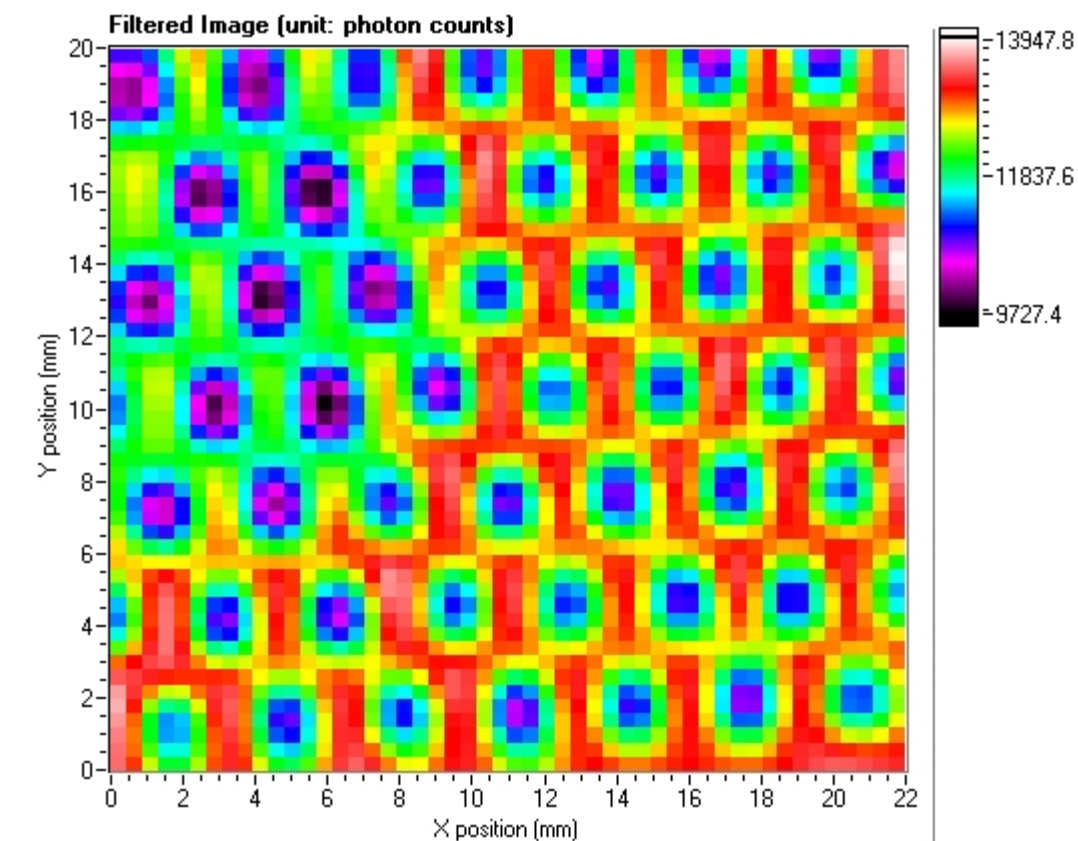
Figure 40. Scan of the 0.5 inch diameter debonding region of Sample #8 - labeled side facing up.
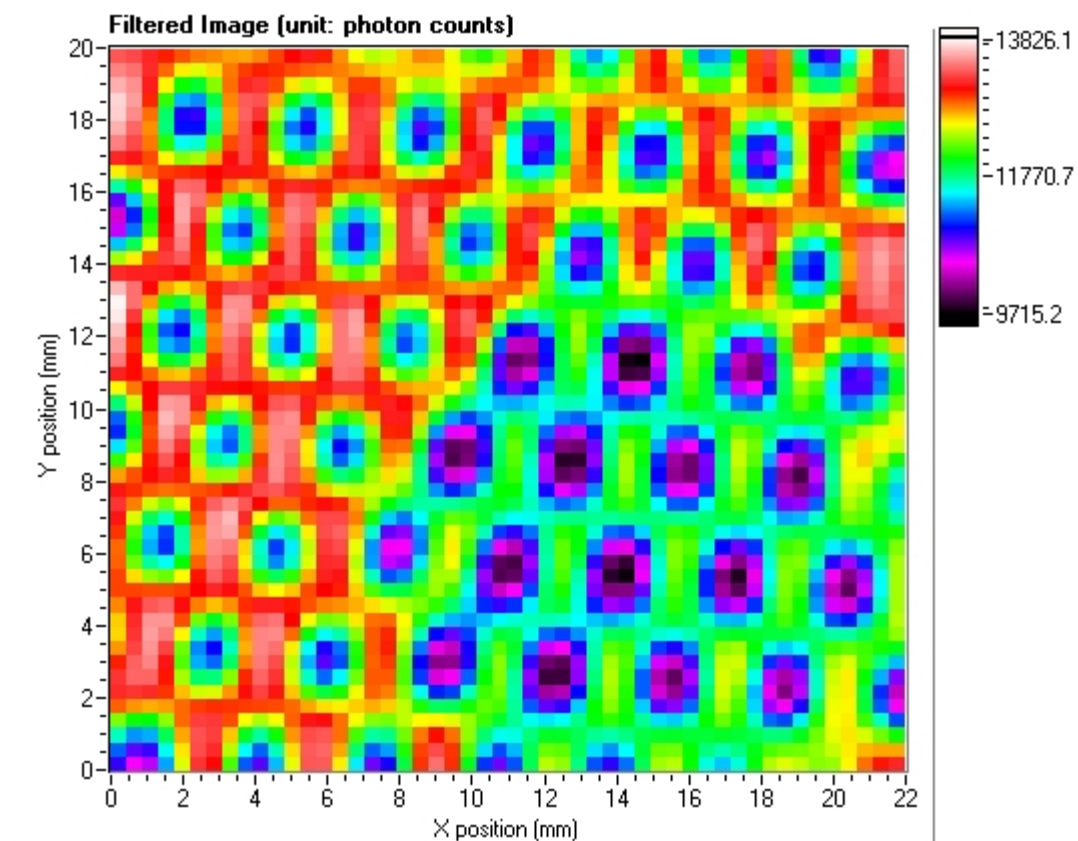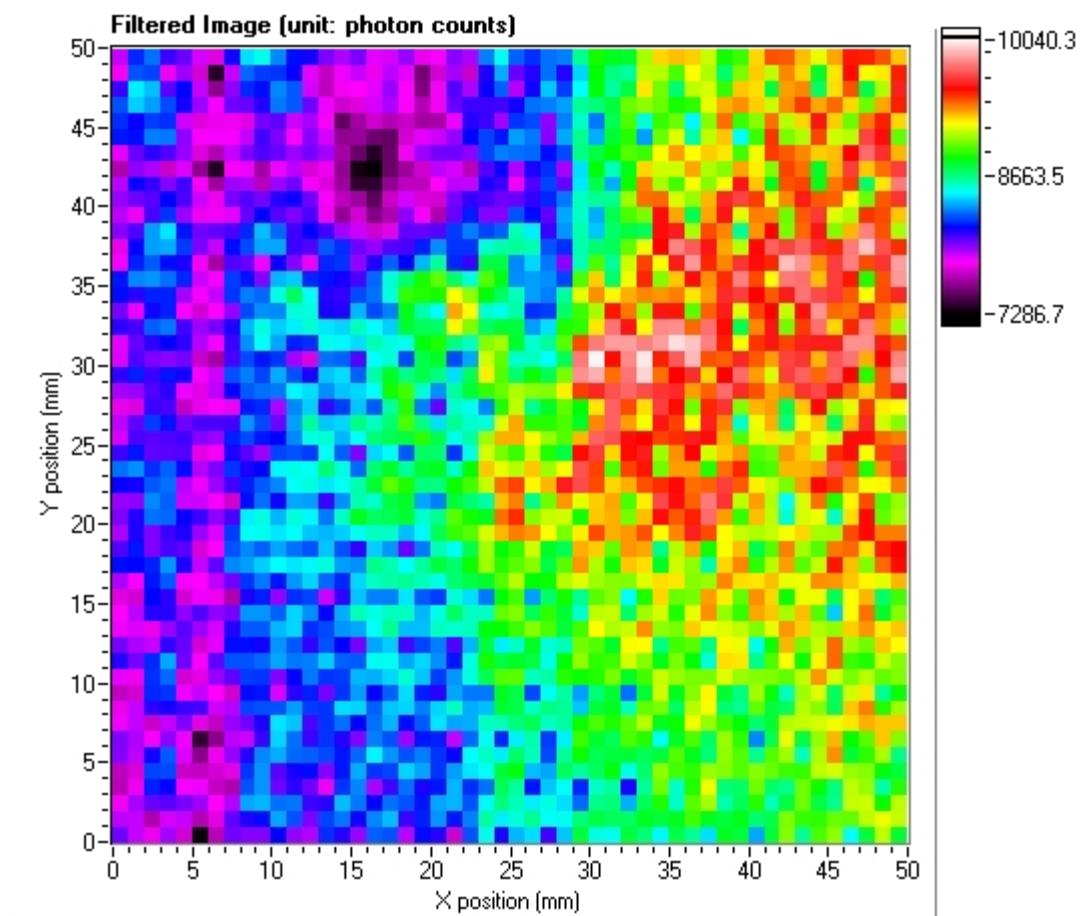
(2 mm X-ray beam spot; 75 kVp and 9 mA; detector 1)

**Figure 41. Scan of the 0.5 inch diameter debonding region of
Sample #8 - labeled side facing down.**

(2 mm X-ray beam spot; 75 kVp and 9 mA; detector 1)

Figure 42. Scan of the crushed core region of Sample #8 - labeled side facing up.

(2 mm X-ray beam spot; 70 kVp and 8 mA; detector 1)

[Crushed core region is the higher intensity
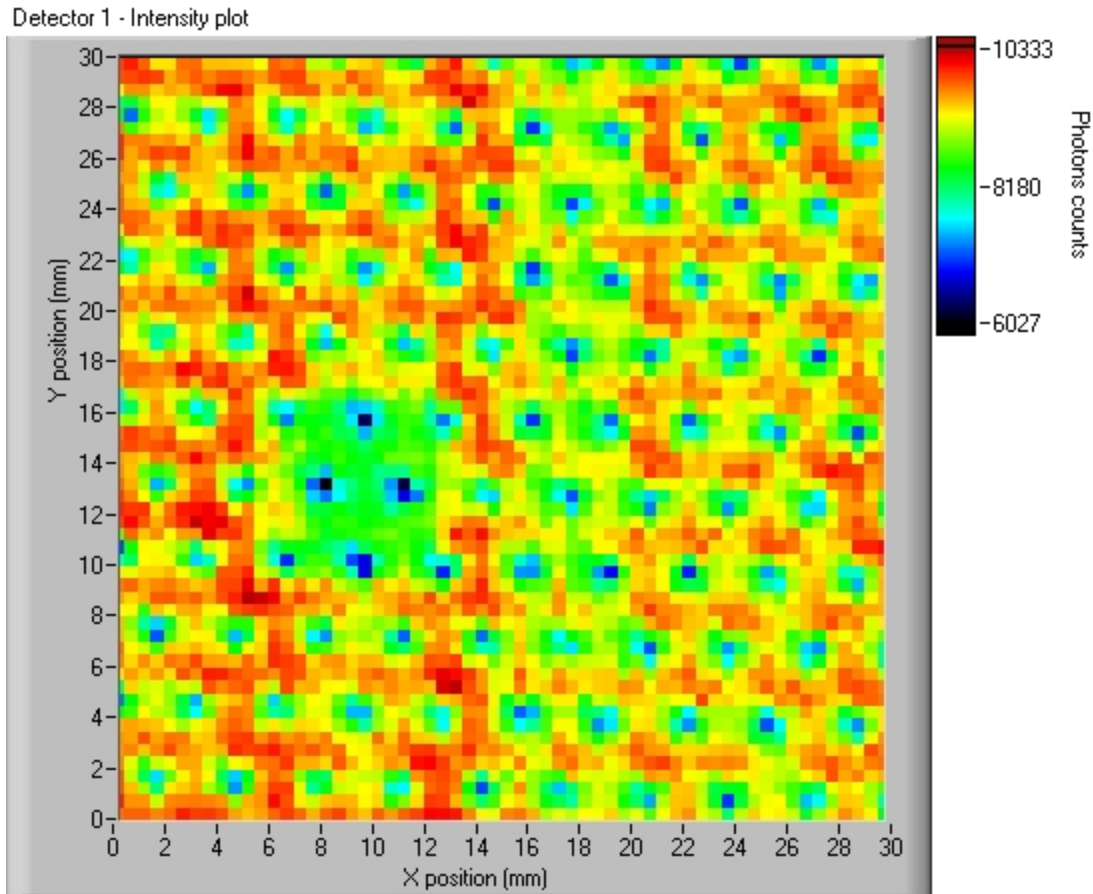area on the right side of the image.]

Figure 43. Unprocessed image of the 0.25 inch diameter debonding region of Sample #8 - labeled side facing up.

(2 mm X-ray beam spot; 70 kVp and 8 mA; detector 1)

[The 0.25 inch (~6 mm) diameter debonding region is seen as the reduced intensity region (green) centered at about x = 10 and y = 13. The scan also shows a vertical region of low intensity centered along a line at about x = 18. This is seen more clearly in the (next) processed image.]
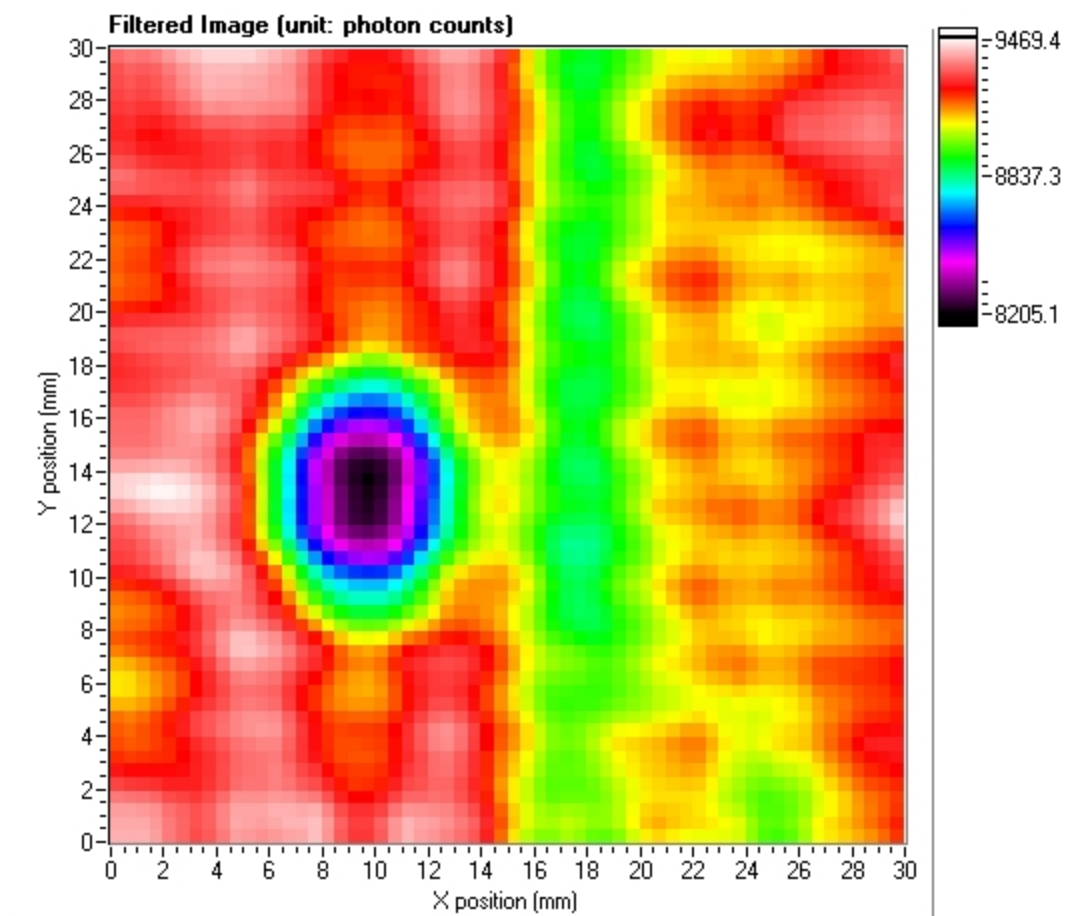
Figure 44. Processed image of the 0.25 inch diameter debonding region of Sample #8 - labeled side facing up.

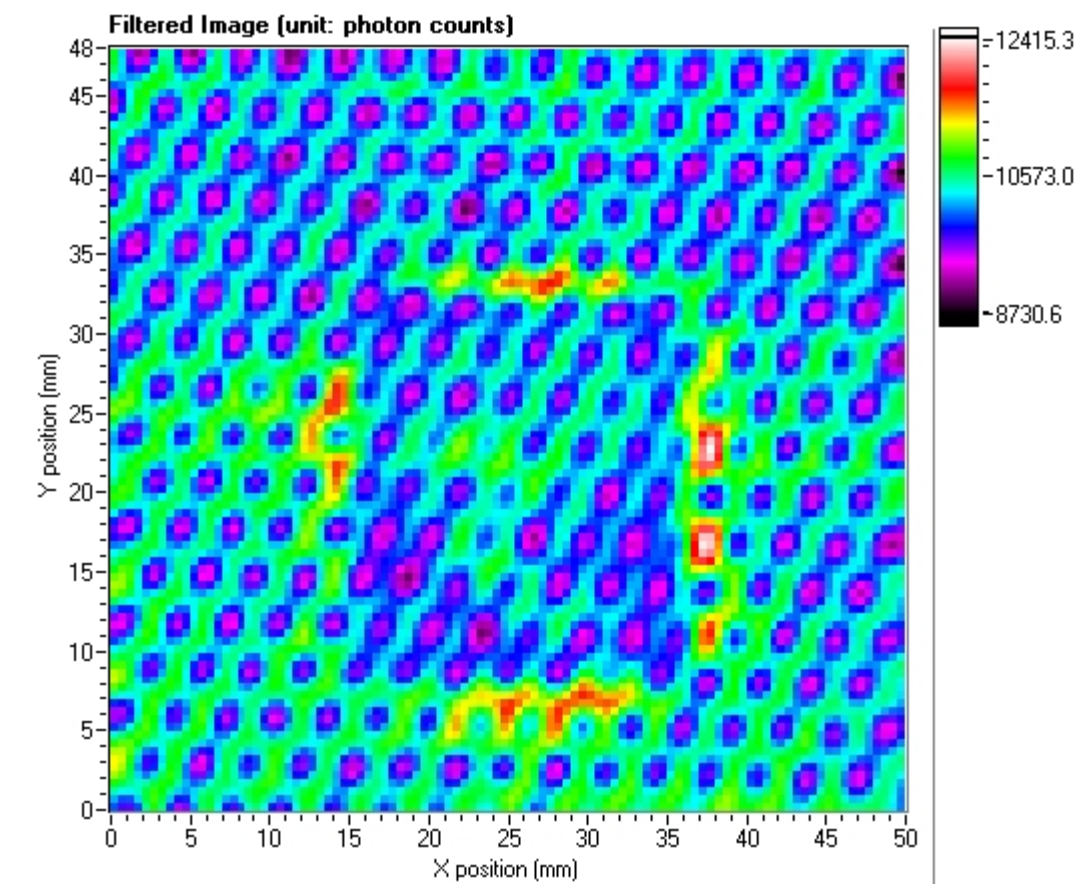(2 mm X-ray beam spot; 70 kVp and 8 mA; detector 1)

Figure 45. Scan of the film region of Sample #8 - labeled side facing down.

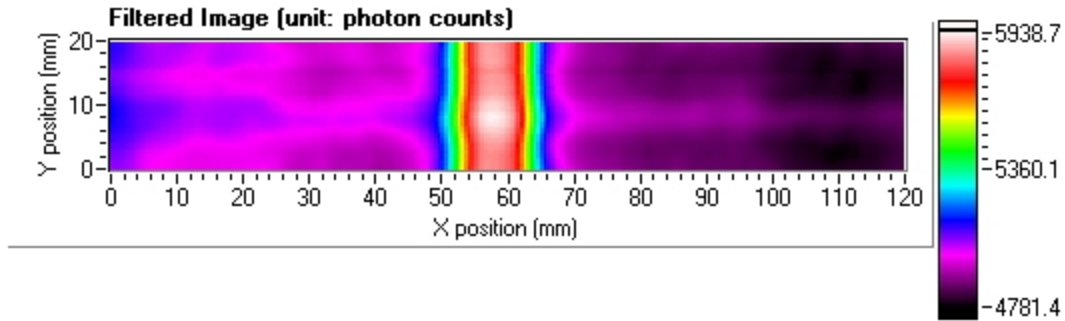(2 mm X-ray beam spot; 75 kVp and 9 mA; detector 1)

Figure 46. Scan of central region of machined aluminum sample plate #2
(2 mm X-ray beam spot; 75 kVp and 8 mA; detector 1)

[Flaw is 10 mm wide, 0,95 mm in height and 3 mm beneath the surface.]
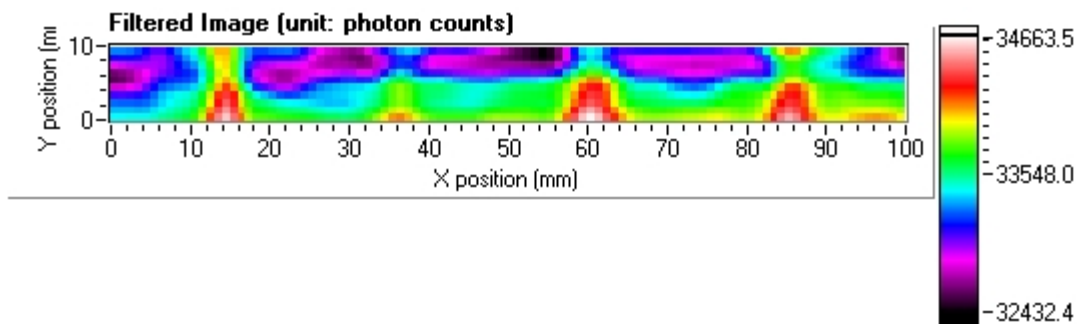

Figure 47. Scan of central region of machined aluminum sample plate #3
(2 mm X-ray beam spot; 75 kVp and 8 mA; detector 1)

flaw 2 (at x ~14 mm) 3 mm wide, 0.5 mm high and 2.5 mm below the surface.
flaw 3 (at x ~36 mm) 1 mm wide, 0.5 mm high and 2.5 mm below the surface.
flaw 4 (at x ~60 mm) 5 mm wide, 0.3 mm high and 2.7 mm below the surface.
flaw 5 (at x ~85 mm) 3 mm wide, 0.3 mm high and 2.7 mm below the surface.